

Magnetic field direction and lunar swirl morphology: Insights from Airy and Reiner Gamma

Doug Hemingway¹ and Ian Garrick-Bethell^{1,2}

Received 21 June 2012; revised 23 August 2012; accepted 30 August 2012; published 30 October 2012.

[1] Many of the Moon's crustal magnetic anomalies are accompanied by high albedo features known as swirls. A leading hypothesis suggests that swirls are formed where crustal magnetic anomalies, acting as mini magnetospheres, shield portions of the surface from the darkening effects of solar wind ion bombardment, thereby leaving patches that appear bright compared with their surroundings. If this hypothesis is correct, then magnetic field direction should influence swirl morphology. Using Lunar Prospector magnetometer data and Clementine reflectance mosaics, we find evidence that bright regions correspond with dominantly horizontal magnetic fields at Reiner Gamma and that vertical magnetic fields are associated with the intraswirl dark lane at Airy. We use a genetic search algorithm to model the distributions of magnetic source material at both anomalies, and we show that source models constrained by the observed albedo pattern (i.e., strongly horizontal surface fields in bright areas, vertical surface fields in dark lanes) produce fields that are consistent with the Lunar Prospector magnetometer measurements. These findings support the solar wind deflection hypothesis and may help to explain not only the general form of swirls, but also the finer aspects of their morphology. Our source models may also be used to make quantitative predictions of the near surface magnetic field, which must ultimately be tested with very low altitude spacecraft measurements. If our predictions are correct, our models could have implications for the structure of the underlying magnetic material and the nature of the magnetizing field.

Citation: Hemingway, D., and I. Garrick-Bethell (2012), Magnetic field direction and lunar swirl morphology: Insights from Airy and Reiner Gamma, *J. Geophys. Res.*, 117, E10012, doi:10.1029/2012JE004165.

1. Introduction

1.1. Background

[2] Although the Moon does not now possess a global magnetic field [Ness *et al.*, 1967], remanent crustal magnetization has been identified on the surface and several stable regional magnetic fields have been detected from orbit [Dyal *et al.*, 1970; Coleman *et al.*, 1972; Lin, 1979; Lin *et al.*, 1998; Hood *et al.*, 2001]. Curiously, many, but not all of these crustal magnetic anomalies are accompanied by sinuous patterns of anomalously high surface reflectance known as swirls [Hood *et al.*, 1979; Hood and Williams, 1989; Richmond *et al.*, 2005; Blewett *et al.*, 2011].

[3] Compared with their surroundings, swirls are optically immature, exhibit spectrally distinct space weathering trends

[Garrick-Bethell *et al.*, 2011], and are depleted in hydroxyl molecules [Kramer *et al.*, 2011]. Swirls appear to overprint local topography, having no detectable topographic or textual expression of their own [Neish *et al.*, 2011]. So far not identified anywhere else in the solar system, swirls are unique natural laboratories where space weathering and crustal magnetism intersect. As such, their study could help address important questions in lunar science including the Moon's dynamo history [Garrick-Bethell *et al.*, 2009; Dwyer *et al.*, 2011; Le Bars *et al.*, 2011], the relative influences of solar wind and micrometeoroid bombardment on space weathering [Hapke, 2001; Vernazza *et al.*, 2009], and the production and distribution of water over the lunar surface [Pieters *et al.*, 2009; Kramer *et al.*, 2011].

[4] Electrostatic migration of dust has been proposed as a possible mechanism for swirl formation [Garrick-Bethell *et al.*, 2011], as have meteoroid or comet impacts [Schultz and Srnka, 1980; Pinet *et al.*, 2000; Starukhina and Shkuratov, 2004]. Another model suggests that crustal magnetic fields act as mini magnetospheres, deflecting the solar wind and protecting portions of the surface from the optical maturation and darkening effects of proton bombardment [Hood and Schubert, 1980; Hood and Williams, 1989]. This paper aims to make and test predictions based on this solar wind deflection model for swirl formation.

¹Earth and Planetary Sciences, University of California, Santa Cruz, California, USA.

²School of Space Research, Kyung Hee University, Yongin, South Korea.

Corresponding author: D. Hemingway, Earth and Planetary Sciences, University of California, 1156 High St., Santa Cruz, CA 95064, USA.
(djheming@ucsc.edu)

©2012. American Geophysical Union. All Rights Reserved.
0148-0227/12/2012JE004165

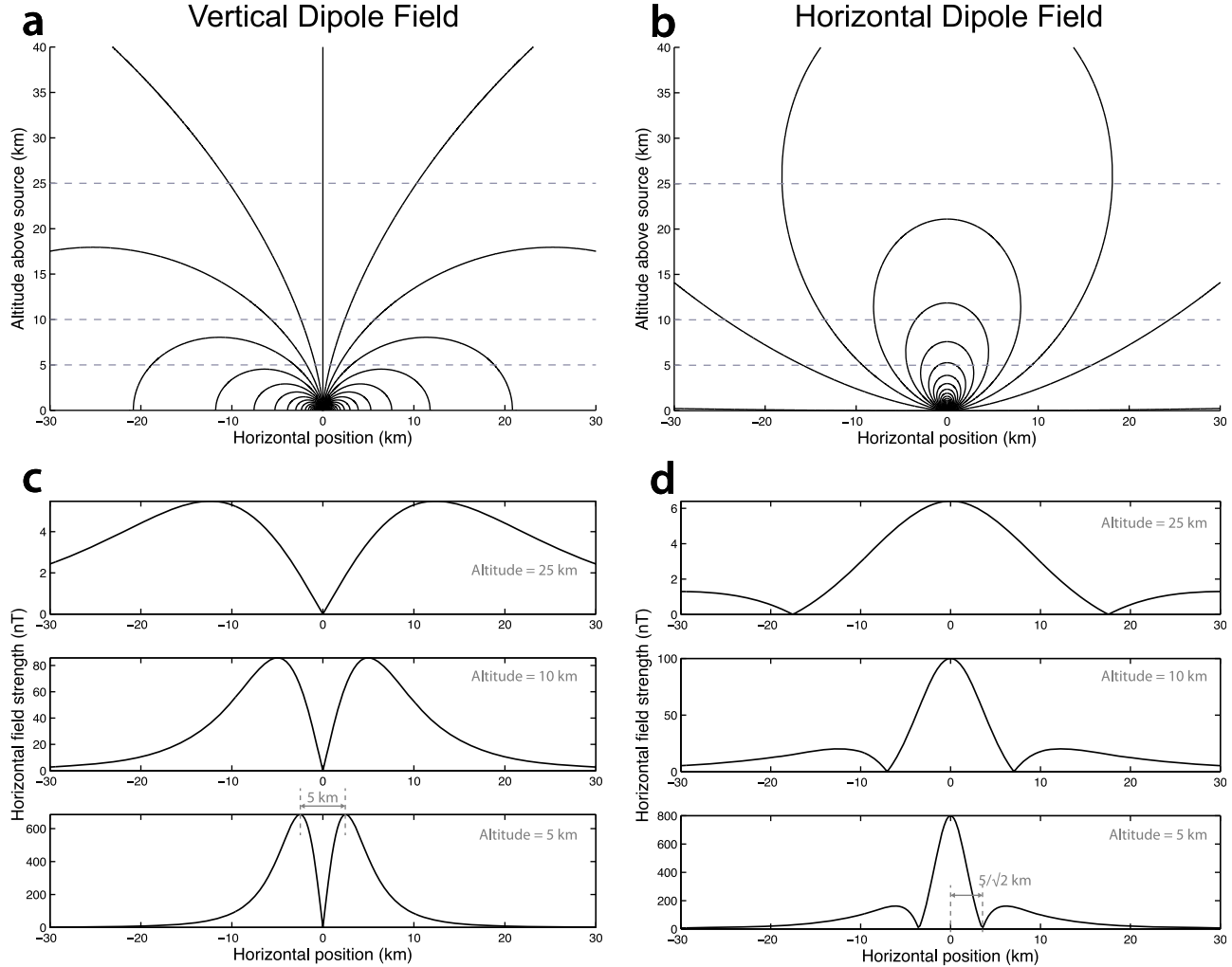


Figure 1. Magnetic field lines due to a single dipole located at the origin and oriented either (a) vertically or (b) horizontally in the plane of the page. (c and d) Profiles of the horizontal component of the magnetic field shown at the various altitudes represented by dashed lines in Figures 1a and 1b. In both cases, the dipolar source has a magnetic moment of 10^{12} Am^2 .

1.2. Predicted Influence of Magnetic Field Direction

[5] The solar wind deflection model suggests that solar wind ions are magnetically deflected due to the Lorentz force. Neglecting the induced electric field, the cross product of particle velocity and magnetic field in the Lorentz Law means the magnetic deflection force is maximized when particle velocity is perpendicular to the magnetic field and zero when it is parallel. Hence, if the high albedo of swirls is the result of inhibited space weathering due to magnetic deflection of solar wind ions, magnetic field direction should influence swirl morphology. While the solar wind incidence angle varies, the ion flux at the surface and thus any darkening effects will be greatest when the ion trajectories are vertical. We therefore predict that portions of the crust that are shielded by dominantly horizontal magnetic fields should receive maximum protection from the solar wind while portions of the crust associated with vertically oriented magnetic fields should experience protection only at low solar wind incidence angles, when darkening effects would be minimal anyway. This suggests that the magnetic fields directly over

the bright swirls should be dominantly horizontal and that away from swirls and in the intraswirl dark lanes, the fields may be either closer to vertical or too weak to offer the surface any protection from solar wind darkening.

[6] Because magnetic field strength decreases rapidly with distance from the source, swirl morphology should depend mainly on the very low altitude structure of the magnetic field. The structure of the field at higher altitudes, where field strength is weaker, has less influence on solar wind deflection. Unfortunately, spacecraft observations are typically limited to higher altitudes and therefore do not directly capture the structure of the near-surface magnetic field. It is therefore important to understand the way in which the field patterns change with observation altitude, including the role that is played by the direction of magnetization. Figure 1 illustrates the magnetic field due to a single dipole that is either vertically oriented (Figures 1a and 1c) or horizontally oriented (Figures 1b and 1d). Figures 1a and 1b illustrate magnetic field lines as seen in vertical cross section while Figures 1c and 1d show profiles of the horizontal component of the magnetic field as observed along the dashed lines

shown in Figures 1a and 1b (in both cases, the model dipole is placed at the origin and arbitrarily assigned a magnetic moment of 10^{12} Am 2). Directly over the vertically oriented dipole, field lines are vertical at any altitude (Figure 1a). Peaks in the horizontal field strength appear to either side and are separated by a distance equal to the observation altitude (Figure 1c). Directly over the horizontally oriented dipole, field lines are horizontal at any altitude (Figure 1b). As the observer moves along an axis parallel to the dipole direction, horizontal field strength decreases, reaching zero (i.e., vertical field lines) at a horizontal distance of $1/\sqrt{2}$ times the observation altitude, before temporarily increasing again slightly (Figure 1d). Appendix A gives a quantitative treatment of the way in which magnetic fields vary with position relative to the source.

[7] Our study uses Lunar Prospector magnetometer data collected at altitudes of ~ 18 km and higher. While we cannot measure the magnetic field structure below these altitudes, we can distinguish between vertically and horizontally oriented magnetizations (we assume that strong crustal magnetic anomalies are approximately dipolar). This means we can select anomalies exhibiting orientations that allow us to test our predictions. Specifically, we can look for intraswirl dark lanes at an anomaly with approximately vertical magnetization because, in that case, field lines should appear vertical at any altitude over the dark lane (Figures 1a and 1c). Likewise, we can look for a correlation between high albedo and strongly horizontal fields at anomalies with approximately horizontal magnetization because field lines at such anomalies should appear horizontal over the brightest areas regardless of observation altitude (Figures 1b and 1d). We find that the Airy anomaly is similar to the case illustrated in Figures 1a and 1c while the Reiner Gamma anomaly is similar to the case illustrated in Figures 1b and 1d.

2. Data Processing

2.1. Lunar Prospector Magnetometer Data

[8] Our study uses Lunar Prospector 3-axis magnetometer measurements (level 1B data) obtained from NASA's Planetary Data System (ppi.pds.nasa.gov). Two distinct approaches are available for producing maps of crustal magnetic fields from orbital measurements. One involves direct mapping using data selected from a sequence of orbits that cross the region of interest [Hood *et al.*, 1981, 2001], resulting in maps of the field at the spacecraft altitude, while the other involves developing a global spherical harmonic model and using it to produce maps at arbitrary altitudes [Purucker and Nicholas, 2010]. The spherical harmonic models are well suited to global mapping and have the advantages of automatically accounting for varying spacecraft altitudes and guaranteeing that the mapped field is a potential field. To date, the best available spherical harmonic models extend to degree 170, corresponding to a horizontal wavelength of ~ 64 km [Purucker and Nicholas, 2010]. However, because we are interested in small-scale swirl morphology, we instead employ a direct mapping technique similar to that of Hood *et al.* [2001], allowing us to map features at wavelengths comparable with the spacecraft altitude (as low as ~ 18 km). As discussed by Hood [2011], the direct mapping approach is suitable for regional mapping and has several advantages including that it allows us to perform model fitting directly to

the minimally processed magnetometer measurements rather than to a derived field model. While we focus here on direct mapping, we did compare our maps against maps we derived from the Purucker and Nicholas [2010] model coefficients. We found that in the latter, crustal anomaly fields appear morphologically similar to the same features in our maps, but are typically broader in horizontal extent and exhibit lower field strength.

[9] Each of our maps incorporates data from a sequence of consecutive orbits that cross the anomaly of interest. The polar orbiting spacecraft obtained global coverage twice each lunation, with consecutive orbits spaced ~ 1 degree in longitude (~ 30 km at the equator) and with along-track measurements recorded at 5-s intervals, corresponding to ~ 8 km spacing in latitude. In order to capture the undisturbed signal of the crustal magnetic anomalies, avoiding times when the field is distorted by the impinging solar wind [Kurata *et al.*, 2005; Purucker, 2008], we use only those magnetometer measurements collected when the Moon was protected from solar wind while passing through the Earth's magnetotail (excluding times when the field was disturbed by the plasma sheet) or when the Moon was in the solar wind but the spacecraft was in the lunar wake (on the dark side of the Moon and away from the terminator by at least 20°). We examined data from the lowest (< 50 km) altitude phase of the mission, between February and July 1999 (the final six months of the mission). The upper portions of Tables 1 and 2 list the 13 orbit sequences we examined for each of the Airy and Reiner Gamma anomalies, respectively. In each case, of the 13 orbit sequences we examined, 5 took place in the lunar wake and 2 in the Earth's magnetotail.

[10] We examined orbit segments spanning 15° of latitude approximately centered on each anomaly. Having eliminated measurements taken outside of wake and tail times, we assume that any remaining external fields are steady over these 15° of latitude and that fields from isolated crustal sources span no more than a few degrees. After subtracting the mean background field, we assume the remaining fields are due to crustal sources. We then convert the spacecraft position into selenographic spherical coordinates, taking the Lunar Orbiter Laser Altimeter reference radius of 1737.4 km [Smith *et al.*, 2010] as zero altitude, and transform the magnetometer measurements into local east, north, and radial components. We next combine data from consecutive orbits to produce magnetic field maps by fitting regular square meshes to the data using Delaunay triangulation. In order to capture the structure of the signal, the grid cells must be no larger than half the spacecraft altitude, which can be as low as ~ 18 km. We therefore use $0.25^\circ \times 0.25^\circ$ (about 7.6 km \times 7.6 km at the equator) as the grid spacing when fitting to the Lunar Prospector magnetometer (LP MAG) data. This grid resolution is also finer than the spacing between the observations (~ 8 km in latitude, up to ~ 30 km in longitude) meaning that no observed signal variations are lost in the gridding process. Using still finer resolution has no effect on the resulting linearly interpolated surface and is undesired as it increases computation time unnecessarily. Conversely, using a larger (more coarse) grid spacing leads to undesired smoothing in latitude, and as cell size approaches 1° , undesired smoothing occurs in longitude as well. Despite our efforts to remove external fields and avoid times with significant field distortion, portions of some of the orbit

Table 1. Lunar Prospector Data Used for Airy^a

Day(s) of 1999	Solar Wind Exposure/Protection	Minimum Solar Zenith Angle (deg)	Mean Altitude (km)	Number of Measurements	Orbit Segments
35,36,37	solar wind	56	27.5	734	15
49,50	wake	131	18.7	772	15
63,64	solar wind	29	28.3	759	14
76,77,78	wake	150	18.5	615	12
90,91	tail	9	28.3	610	11
104,105	wake	151	18	678	13
117,118	tail	26	28.3	776	14
131,132	wake	134	34.4	782	14
145,146	solar wind	52	38.5	838	15
158,159	wake	111	34.3	627	12
172,173	solar wind	77	38.6	824	15
186,187	solar wind	88	35.9	660	12
199,200	solar wind	102	37	785	14
131,132	wake	136	34.4	48	4
91,118	tail	15	28.4	82	7
49,50,77,104	wake	134	18.5	130	12

^aThe upper part of the table lists the 13 orbit sequences (each consisting of segments of between 11 and 15 consecutive orbits) we examined in a $15^\circ \times 15^\circ$ window centered on the anomaly. The last three rows of the table show the 260 measurements retained after discarding data collected outside of wake and tail times, after combining like-altitude orbit sequences, and after cropping to a $3.25^\circ \times 4^\circ$ study area.

sequences still appear to be contaminated by transient signals and are therefore discarded. In order to obtain maps with improved spatial coverage, we combine measurements from different orbit sequences if the observation altitudes are sufficiently similar (differing by less than ~ 1 km). Since the spacecraft altitude varies only slightly (<1 km) over the scale of our maps (>120 km), we do not perform upward or downward continuation of the signal to some fixed altitude. Instead, our maps represent the magnetic field at the slowly varying spacecraft altitude. Finally, we define study areas within the boundaries of the processed data: the Airy study area is illustrated in Figures 2a–2c while the Reiner Gamma study area is illustrated in Figures 2d–2f. As summarized in the lower portions of Tables 1 and 2, this results in Airy study area maps at altitudes of ~ 18 km, ~ 28 km, and ~ 34 km, using a total of 260 LP MAG measurements, and Reiner Gamma study area maps at altitudes of ~ 18 km, ~ 34 km, and ~ 40 km, using a total

of 245 LP MAG measurements (only the lowest altitude maps are presented here).

2.2. Clementine Reflectance Mosaics

[11] Our study uses Version 2 Clementine 750 nm reflectance mosaics produced by the USGS (United States Geological Survey) map-a-planet service (www.mapaplanet.org). Compared with the Version 1 (V1) maps, the Version 2 (V2) maps use a newer geodetic control network [Archinal *et al.*, 2006], refining the horizontal registration by as much as 10 km in some locations. We have manually adjusted the V2 reflectance values to match those of the V1 maps, which have been more carefully controlled to represent true reflectance.

3. Observations

[12] We focus our discussion here on two specific examples: Airy and Reiner Gamma. The Airy anomaly exhibits a

Table 2. Lunar Prospector Data Used for Reiner Gamma^a

Day(s) of 1999	Solar Wind Exposure/Protection	Minimum Solar Zenith Angle (deg)	Mean Altitude (km)	Number of Measurements	Orbit Segments
40,41	solar wind	51	27.7	820	15
54,55	wake	139	19	769	14
67,68	solar wind	24	28.5	832	15
81,82	wake	162	18.6	795	15
95,96	solar wind	3	28.6	834	16
108,109	wake	158	18.3	634	12
122,123	solar wind	29	28.5	833	15
136,137	wake	135	34.8	703	13
149,150	tail	56	39.3	817	15
163,164	solar wind + wake	109	34.5	798	15
177,178	solar wind + tail	82	39.4	842	15
190,191	solar wind	83	36.3	838	15
204,205	solar wind	107	37.7	769	14
150	tail	57	39.7	48	4
136,163,164	wake	110	34.3	79	7
54,81,82,109	wake	141	18.3	118	10

^aThe upper part of the table lists the 13 orbit sequences (each consisting of segments of between 12 and 16 consecutive orbits) we examined in a $15^\circ \times 15^\circ$ window centered on the anomaly. The last three rows of the table show the 245 measurements retained after discarding data collected outside of wake and tail times, after combining like-altitude orbit sequences, and after cropping to a $3.25^\circ \times 4^\circ$ study area.

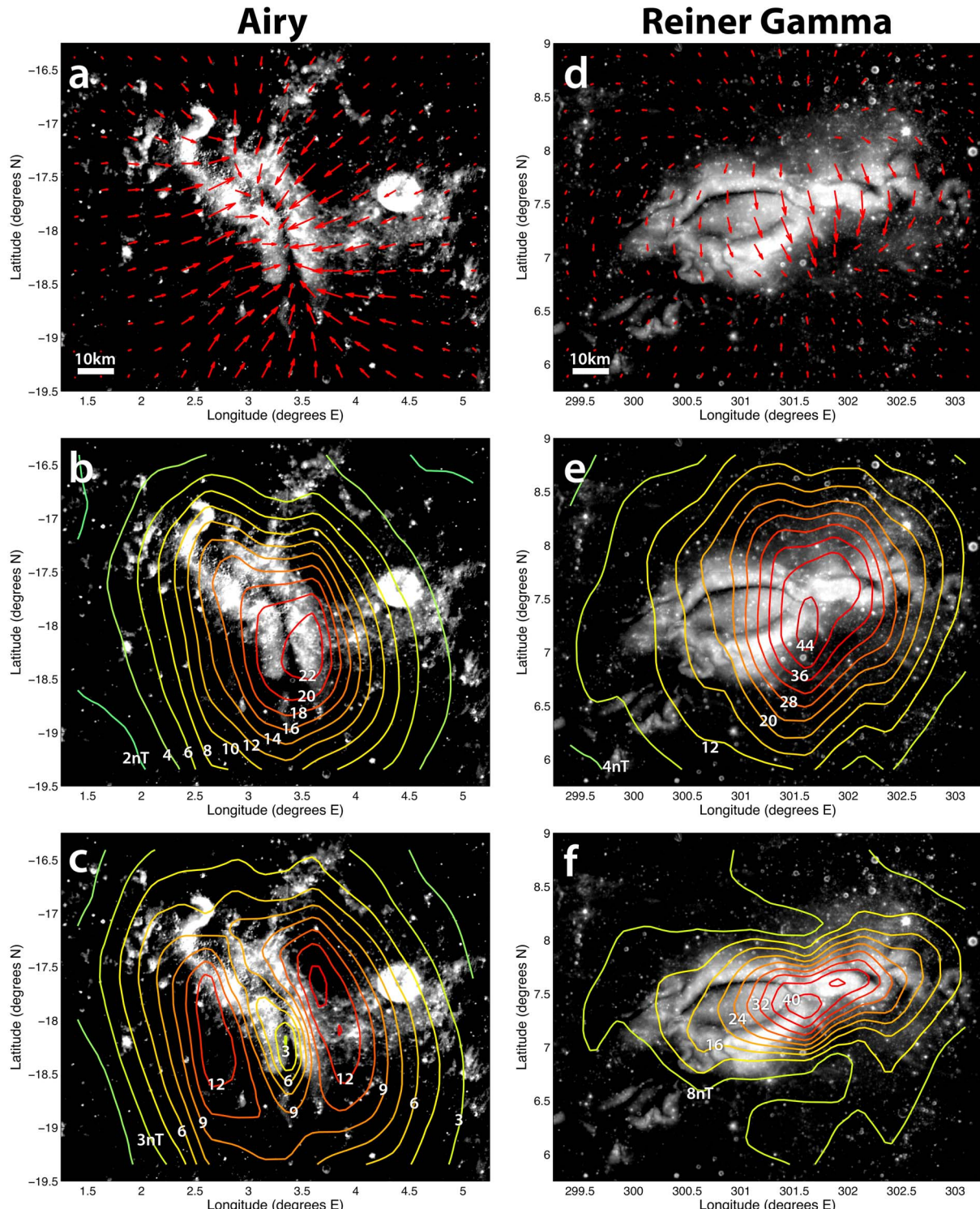


Figure 2. Magnetic field maps derived from Lunar Prospector magnetometer data over Clementine 750 nm reflectance maps at the (a–c) Airy and (d–f) Reiner Gamma anomalies. Figures 2a and 2d show the direction of field lines at the spacecraft altitude (~ 18 km in both cases), with arrow lengths showing relative horizontal field strength. Figures 2b and 2e show contours of the total magnetic field strength, and Figures 2c and 2f show contours of the horizontal component alone. The Airy maps shown here are derived from LP MAG data collected on days 49–50, 77, and 104 of 1999 while the Reiner Gamma maps are derived from data collected on days 54, 81–82, and 109 of 1999.

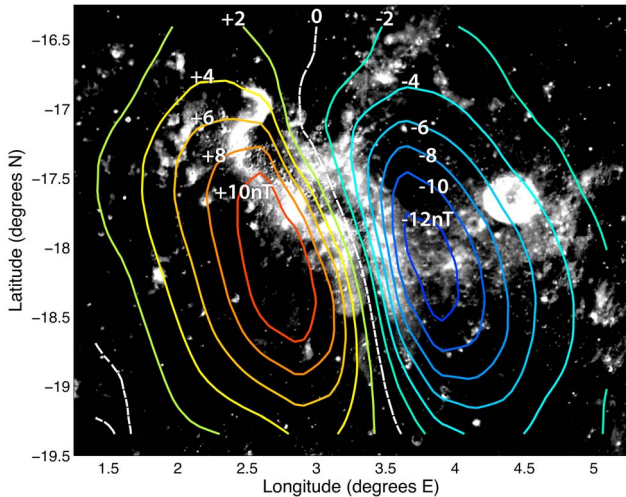


Figure 3. East-west component of magnetic field as measured by Lunar Prospector over Clementine 750 nm reflectance at Airy. Contour line colors and labels indicate magnitude of eastward field strength, with warm colors indicating east-pointing fields and cool colors indicating west-pointing fields. The dashed white line indicates zero field strength in the east-west direction. The map is derived from LP MAG data collected on days 49–50, 77, and 104 of 1999.

magnetic field resembling the case illustrated in Figure 1a while the Reiner Gamma anomaly field resembles the case illustrated in Figure 1b. The distinct orientations of these two anomalies reveal different aspects of the relationship between magnetic field direction and swirl morphology.

3.1. Airy

[13] First described by Blewett *et al.* [2007], the Airy swirl is found near Airy crater in the lunar nearside highlands. At the Lunar Prospector spacecraft altitude, the magnetic field lines tend to point inward toward the middle of the anomaly, becoming increasingly vertical and downward pointing at the center (Figure 2a), consistent with a source magnetization that is pointed mainly downward. This inferred magnetization direction is based on examination of the vector components and is supported by the models described in section 4. Here, contour maps of the total magnetic field strength illustrate only that the albedo anomaly is approximately centered on the magnetic anomaly (Figure 2b). However, maps of the horizontal field alone (Figure 2c) reveal structure that is more closely related to albedo morphology. For example, the dark lane through the center of the albedo anomaly forms an approximate plane of symmetry in the observed horizontal magnetic field map. Even more striking is the alignment between the dark lane in the center of the anomaly and the line representing zero east-west magnetic field strength (dashed white line in Figure 3). The brightest parts of the swirl are organized into two roughly parallel lobes on either side of the dark lane. The center-to-center horizontal distance between the lobes is approximately 8–10 km. Peaks in the horizontal field strength are also organized into two lobes on either side of the dark lane but with a peak-to-peak separation of roughly 30 km (Figure 2c). As illustrated in Figure 1c, a closer spacing of horizontal

field strength peaks is expected at lower altitudes, potentially allowing for better alignment with the swirl's bright lobes.

3.2. Reiner Gamma

[14] Reiner Gamma, the type example for lunar swirls, is found in Oceanus Procellarum near the western limb of the lunar nearside. At the Lunar Prospector spacecraft altitude, the magnetic field lines are south pointing (Figure 2d), consistent with a source magnetization that is mainly horizontal and north pointing. This inferred magnetization direction is based on examination of the vector components, is supported by the models described in section 4, and is in agreement with Kurata *et al.* [2005]. Contour maps of total magnetic field strength, seen here (Figure 2e) and elsewhere [e.g., Hood *et al.*, 2001], illustrate only that the albedo anomaly is approximately co-located with the magnetic anomaly; there is no clear relationship between total field strength and the morphology of the albedo anomaly. However, contour maps of the horizontal component alone (Figure 2f) show that regions of high horizontal field strength correspond well with the bright swirl. Based on SELENE magnetometer data, Shibuya *et al.* [2010] have reported similar findings for Reiner Gamma and other anomalies. Patches of high albedo tend not to occur where fields are weak, or where fields are strong but lack a large horizontal component. This observation is consistent with the hypothesis that darkening due to solar wind ion bombardment will be minimized where magnetic fields are strongly horizontal.

[15] We tested the degree to which magnetic field direction is related to reflectance by measuring the correlation between reflectance and the angle the field makes with the vertical. Figure 4 plots reflectance versus magnetic field direction using data points gathered from all six retained sets of LP

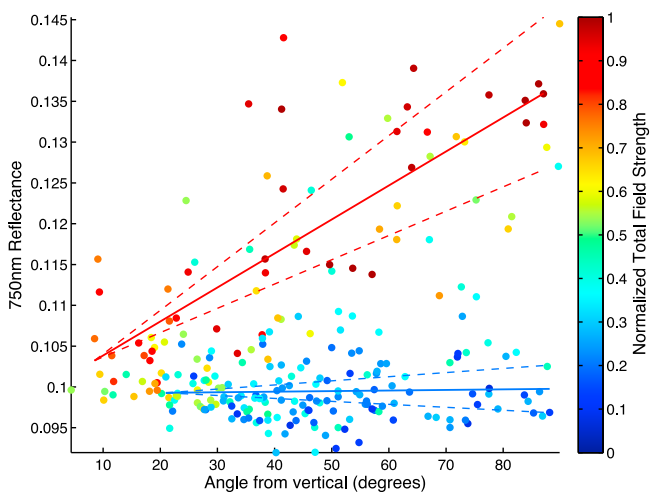


Figure 4. Correlation between magnetic field direction and reflectance at Reiner Gamma. ‘Angle from vertical’ is 90° where field lines are horizontal. Data points are color-coded by total field strength with cool colors representing weak fields and warm colors representing strong fields. Blue and red regression lines are fit to the weakest and strongest thirds of the data points, respectively, demonstrating that magnetic field direction becomes increasingly important with increasing field strength.

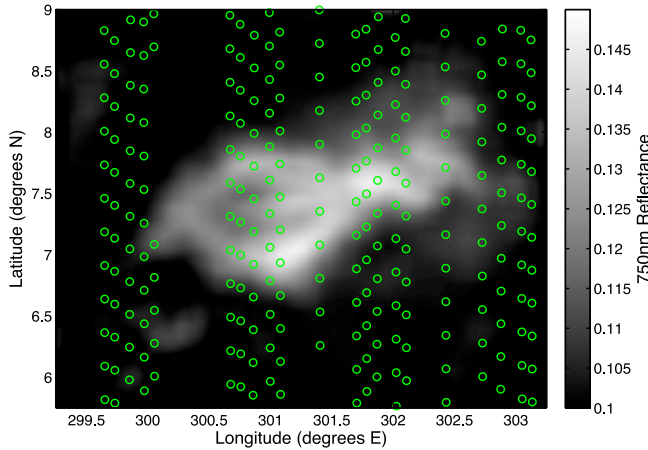


Figure 5. Locations of the 245 LP MAG data points (green circles) used to generate Figure 4. Background is a Clementine 750 nm reflectance mosaic with resolution reduced to be comparable with the LP MAG data resolution.

MAG measurements. Since the field strength varies with altitude, values were normalized to the maximum total field strength for each map before being combined into the set of 245 data points used to generate the scatterplot. Figure 5 illustrates the locations of the data points and corresponding reflectance values used to make the scatterplot. The reflectance map in Figure 5 has been smoothed by a $0.25^\circ \times 0.25^\circ$ window moving average filter in order to reduce its effective resolution to be comparable to the LP MAG data resolution. This removes the high frequency component of the albedo signal that could not possibly be captured in the lower frequency magnetic field data. The data points in Figure 4 are color-coded according to normalized total field strength. Cool colors represent weak fields and warm colors represent strong fields. A blue regression line is fit to the weakest third of the data points and illustrates that, as expected for weak fields, reflectance values are low regardless of magnetic field direction. A red regression line is fit to the strongest third of

the data points and illustrates that, for stronger fields, reflectance values are low where field lines are vertical and high where field lines are horizontal. Dashed lines are used to show 95% confidence intervals on the estimated slopes, indicating that the observed differences in slope are statistically significant. These trends are precisely what we would expect if the albedo anomalies owe their brightness to magnetic deflection of solar wind.

3.3. Discussion

[16] The examples of Airy and Reiner Gamma illustrate distinct aspects of the solar wind deflection phenomenon: the Airy case shows that dark lanes may be associated with vertical magnetic fields (Figures 2a–2c and Figure 3), while the Reiner Gamma example demonstrates that bright areas may be associated with strongly horizontal fields (Figures 2d–2f and Figure 4). In principle, however, both of these effects should be present at both locations. That is, we should expect to see alignment between the bright lobes of Airy and peaks in horizontal magnetic field strength and we should expect to see vertical field lines over the dark lanes of Reiner Gamma. But as discussed in section 1.2, we expect the near-surface field patterns to dominate solar wind deflection and we do not yet have observations at sufficiently low altitudes to map the near-surface field directly. However, we can use source models to determine whether the near surface field pattern we predict (horizontal over bright areas and vertical over dark lanes) is consistent with the observational constraints we do have.

4. Source Modeling

[17] Using a combination of techniques, including a genetic search algorithm, we developed subsurface magnetization source models to gain insight into the possible distribution of source material at the Airy and Reiner Gamma anomalies. We use these models to support our interpretation of the observations discussed above and to allow us to further test the plausibility of our hypothesis—that areas of high albedo should coincide with dominantly horizontal near-surface magnetic fields.

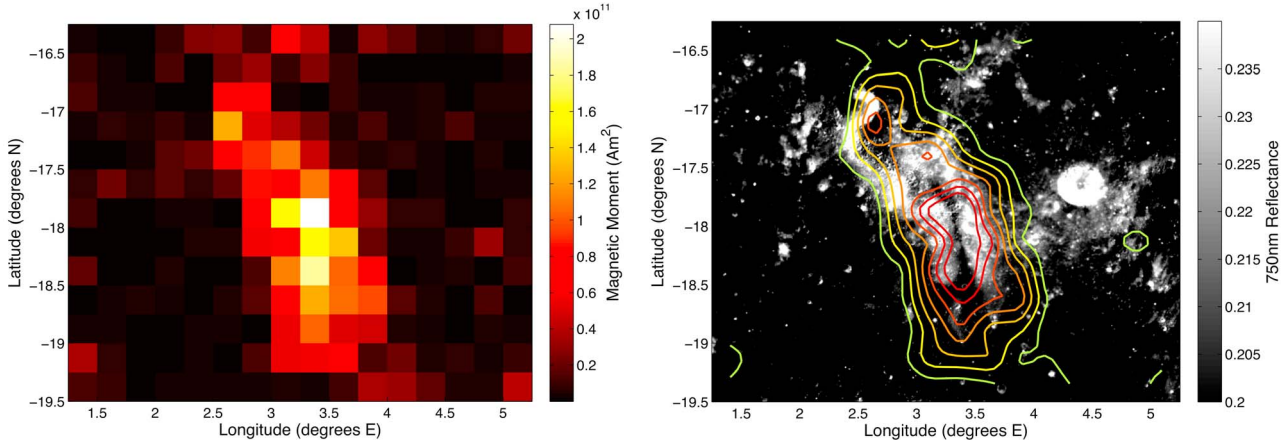


Figure 6. The Airy source model obtained via the genetic search algorithm described in section 4.1.1. (left) Each square represents a single dipole covering $0.25^\circ \times 0.25^\circ$ (roughly $5.5 \times 10^7 \text{ m}^2$) with the color indicating each dipole's total magnetic moment (typical values in the center are $1.25 \times 10^{11} \text{ Am}^2$ per dipole). (right) The same information as contours over Clementine albedo, suggesting approximate agreement between the source structure's longitudinal axis and that of the swirl's dark lane.

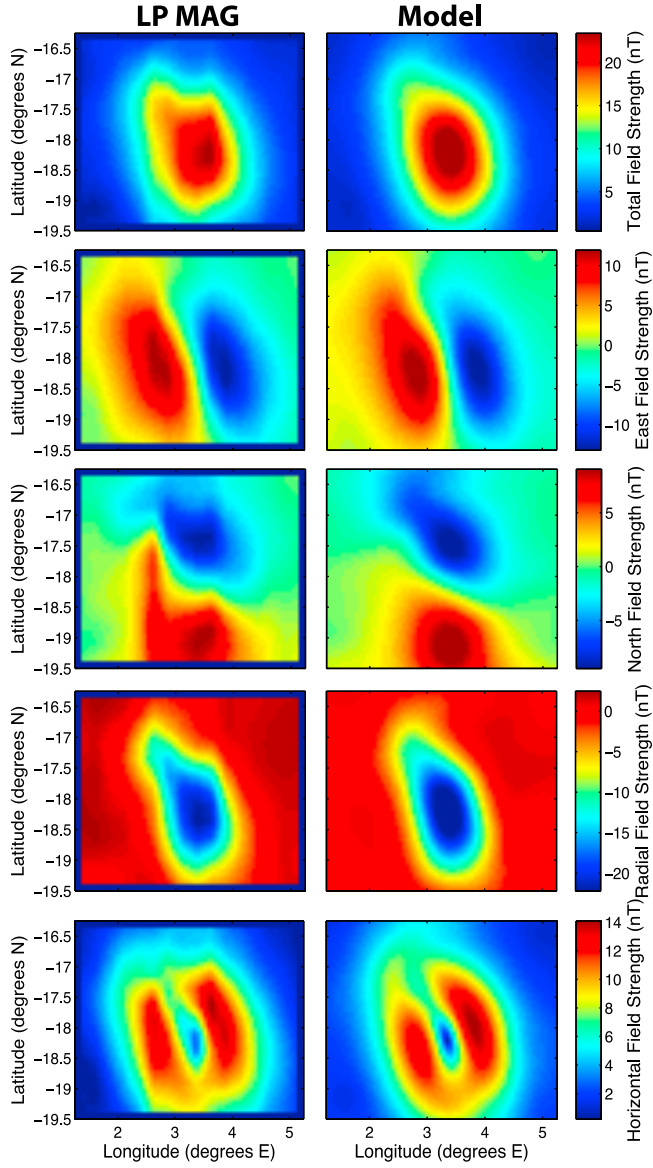


Figure 7. Comparison of (left) the observed field at ~ 18 km over Airy (derived from LP MAG data collected on days 49–50, 77, and 104 of 1999) and (right) the model field (obtained by fitting a grid of dipoles to the LP MAG data using the algorithm described in Appendix B).

4.1. Lunar Prospector Data Fitting

[18] As a first step, we use the Lunar Prospector magnetometer (LP MAG) measurements to determine the most probable characteristics of the magnetic source (the approximate distribution of magnetic material as well as the magnetic moment magnitude and orientation). The results are spatially coarse as the data are insensitive to variations on scales smaller than the observation altitudes. The results are also inherently non-unique as trades can be made between depth and magnetic moment magnitude, for example. Previous studies have modeled the source of the central part of the Reiner Gamma anomaly as a single dipole [Kurata *et al.*, 2005] or as a grid of dipoles [Nicholas *et al.*, 2007] using inversion techniques [Von Frese *et al.*, 1981; Purucker *et al.*,

1996; Dymant and Arkani-Hamed, 1998; Parker, 2003] to obtain models that best fit the LP MAG data in a least squares sense. Here, we employ an alternative approach involving iterative forward modeling to identify the characteristics of the best fitting solutions. Our approach demonstrates that a range of different solutions can deliver similarly good results. Throughout our modeling, we make the simplifying assumption that the source material is coherently magnetized in a single direction; much larger remanent magnetizations would be required to produce the observed fields if the source materials were not unidirectionally magnetized, and the inferred values are already large (as discussed in section 5.1).

4.1.1. Airy Model

[19] We begin with a single dipole model to find the magnetic moment direction that best fits, in a least squares sense, the 260 LP MAG measurements of the Airy study area. We define the ‘effective error’ at each data point as the maximum of the three vector component residuals. The least squares solution thus minimizes residuals in all three vector components simultaneously. We vary the burial depth from 0 to 20 km in 1-km increments and the magnetic moment magnitude from 0 to 8×10^{12} Am 2 in increments of 5×10^{11} Am 2 . We vary the inclination (angle positive downward from the horizontal) from -90° to $+90^\circ$ and the declination (angle positive clockwise from north) through 360° , each with 1° resolution. We find the measurements are well accommodated by a dipole buried between 10 and 20 km below the surface, with magnetic moment magnitude between 4×10^{12} Am 2 and 7×10^{12} Am 2 , inclination between 79° and 81° and declination between -14° and $+29^\circ$ (i.e., pointed steeply downward and slightly to the north). Since this method delivers equally good solutions over a wide range of depths and magnetic moment magnitudes, we do not attempt to constrain depth and magnitude at this stage. In any case, because we are assuming a single dipole, the model fit overestimates the true source depth.

[20] Next, we expand the parameter space by replacing the single dipole with a grid of dipoles, separated by 0.25° in both latitude and longitude (a distance comparable with half the minimum spacecraft altitude), resulting in a total of 208 dipoles. We allow each of the 208 dipoles’ magnitudes to vary independently. We allow the burial depth of the grid to vary as a whole but burial depth does not vary between dipoles and we do not allow the dipoles to be above the lunar surface. Likewise, we allow the magnetization direction to vary as a whole but direction does not vary between dipoles. This opens a parameter space that is too large to explore completely, even with coarse resolution. Instead, we employ a genetic search algorithm that iteratively adjusts each of the 211 independent parameters (208 independent dipole moment magnitudes plus depth of the grid, inclination and declination), gradually progressing toward improving least squares solutions (Appendix B gives a thorough description of the algorithm). Based on the single dipole model fit described above, we initiate the genetic search algorithm with a downward pointing magnetization (80° inclination, 8° declination) and an arbitrary burial depth of 10 km. Again, the algorithm attempts to find a solution that minimizes the sum of squares over the ‘effective’ error at each of the 260 LP MAG data points. The dipoles in the final model grid have inclination 79° , declination 20° and a total magnetic moment of 4.7×10^{12} Am 2 distributed as shown in Figure 6. The final

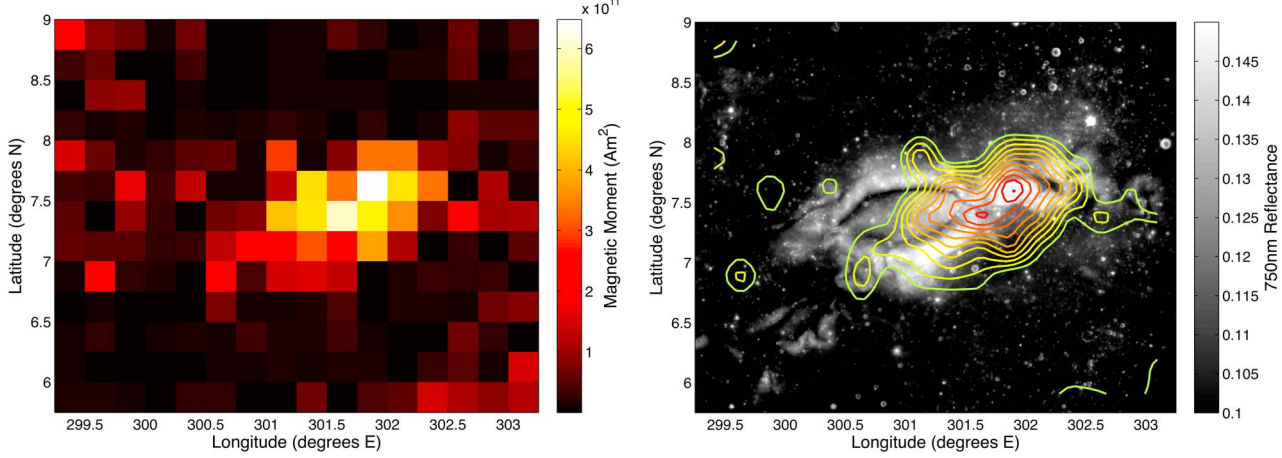


Figure 8. The Reiner Gamma source model obtained via the genetic search algorithm described in section 4.1.2. (left) Each square represents a single dipole covering $0.25^\circ \times 0.25^\circ$ (roughly $5.7 \times 10^7 \text{ m}^2$) with the color indicating each dipole's total magnetic moment (typical values in the center are $\sim 3.4 \times 10^{11} \text{ Am}^2$ per dipole). (right) The same information as contours over Clementine albedo.

grid has a burial depth of ~ 650 m, but again, depth is not well constrained by the LP MAG data as it can be traded against magnetic moment magnitude and the lateral extent of the source; an equally good fit could be obtained with a source that is deeper, stronger and more horizontally concentrated. Although the model is spatially coarse, the distribution of magnetic moments appears to be consistent with a source structure that is centered on the anomaly and elongated in a north-south direction. Figure 7 shows that the resulting model field compares very well with the observed field. The magnetization direction is close to that of the hypothetical field illustrated in Figure 1a, indicating that the intraswirl dark lane may well coincide with vertical field lines at the surface.

4.1.2. Reiner Gamma Model

[21] Again, we begin with a single dipole oriented so that it best fits, in a least squares sense, the 245 LP MAG measurements at the Reiner Gamma study area. Using the ‘effective’ error metric described for the Airy model above, we search for the least squares best fit by varying the burial depth from 0 to 20 km in 1-km increments, the magnetic moment magnitude from 0 to $2 \times 10^{13} \text{ Am}^2$ in increments of 10^{12} Am^2 , the inclination from -90° to $+90^\circ$ and the declination through 360° , with 1° resolution for both inclination and declination. We find that the measurements are well accommodated by a dipole that is buried between 8 and 15 km below the surface with magnetic moment between $9 \times 10^{12} \text{ Am}^2$ and $16 \times 10^{12} \text{ Am}^2$, inclination between -6° and $+5^\circ$ and declination between -18° and -3° (i.e., lying approximately in the plane of the lunar surface and pointing slightly west of north). For comparison, Kurata *et al.* [2005] modeled this part of the anomaly as a single dipole buried 11.1 km below the surface with magnetic moment $11.3 \times 10^{12} \text{ Am}^2$, inclination $+1.3^\circ$ and declination -11° . Once again, depth and magnitude are not well constrained by the data and are overestimated by this single dipole model.

[22] As with the Airy model, we next expand the parameter space by replacing the single dipole with a grid of 208 dipoles and use the genetic algorithm described in Appendix B to find a solution that best fits the 245 LP MAG data points. The

final model dipole grid is magnetized with inclination $+4^\circ$ and declination -12° at a depth of 1.6 km (but again, depth is not well constrained by the LP MAG data), and has total magnetic moment $\sim 1.4 \times 10^{13} \text{ Am}^2$ distributed as shown in Figure 8. The source model is spatially coarse but is consistent with a source structure that is elongated in the east-west direction and is most intense in the brightest part of the albedo anomaly. Figure 9 shows that the resulting model field compares well with the observed field. For comparison, Nicholas *et al.* [2007] modeled the Reiner Gamma source as a grid of dipoles separated by 0.1° and placed at the surface, coincident with the albedo anomaly. Those authors assumed a northward magnetization and solved for the magnitude and sign at each of the dipoles, obtaining the distribution of magnetization illustrated in Figure 10. In spite of the very different methods employed, the two results resemble one another, predicting strong magnetization in the brightest parts of the anomaly.

4.2. Albedo Pattern Matching

[23] The results of the genetic search algorithm suggest that the distribution of the underlying source material coincides roughly with the shape of the albedo anomaly: a north-south distribution for Airy and an east-west distribution for Reiner Gamma. Here, we refine our source models by applying the constraint that the near-surface field be structured according to our hypothesis: strongly horizontal over the brightest parts of swirls and vertical in the intraswirl dark lanes. This allows for greatly improved spatial resolution since Clementine reflectance mosaics are available at 256 pixels/degree whereas LP MAG data are limited to $\sim 1\text{--}4$ pixels/degree. If our hypothesis is correct, source models constrained by the albedo pattern should produce fields that are consistent with the LP MAG observations made at higher altitudes. Below, we show that even simple source models are sufficient to accomplish this, suggesting that our models are highly plausible.

4.2.1. Airy Model

[24] Given the downward-pointing magnetization at Airy (section 4.1.1) and the associated field pattern (Figure 1c),

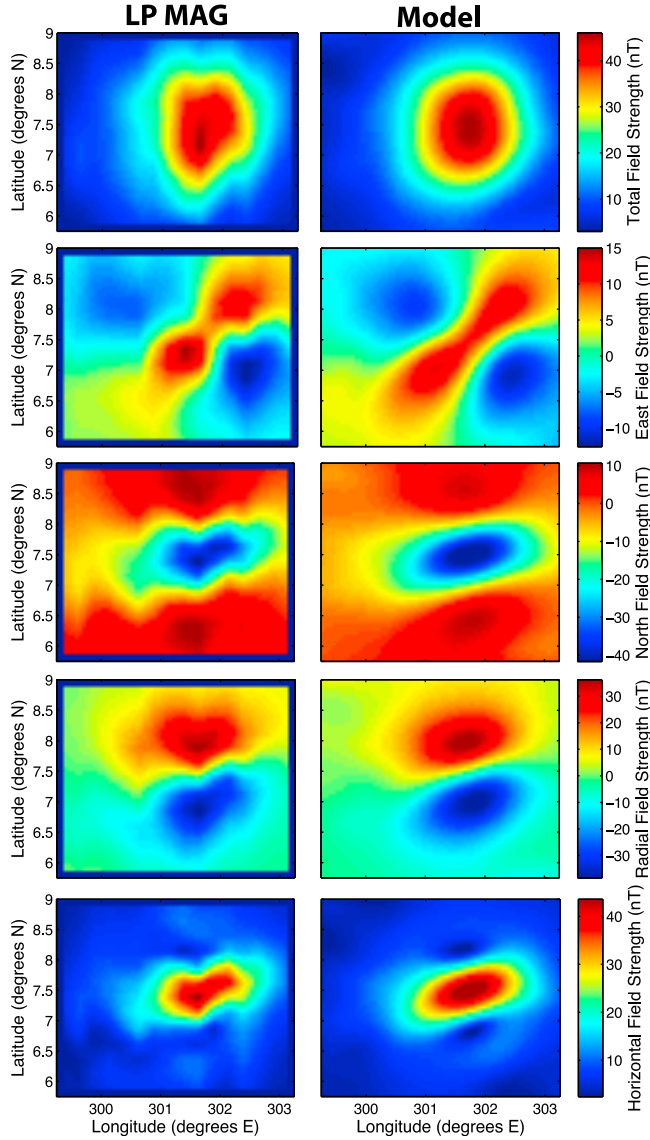


Figure 9. Comparison of (left) the observed field at ~ 18 km over Reiner Gamma (derived from LP MAG data collected on days 54, 81–82, and 109 of 1999) and (right) the model field (obtained by fitting a grid of dipoles to the LP MAG data using the algorithm described in Appendix B).

the morphology of the Airy swirl suggests a roughly linear source structure following the dark lane. In order to be consistent with our hypothesis, the vertically magnetized source material cannot substantially underlie the bright lobes since this would mean vertical field lines in bright areas. We therefore replace the grid of dipoles described in section 4.1.1 with an array of 32 dipoles arranged as a two-segmented linear feature following the dark lane (Figure 11, left). In cross-section, the field pattern from such a line source resembles the pattern from a single dipole (illustrated in Figures 1a and 1c). However, for a linear source, the peaks in the horizontal field profile are shifted outward slightly such that the peak-to-peak separation is $2/\sqrt{3}$ times the altitude above the source rather than being equal to the altitude above the source (details are given in Appendix A). If we assume the two bright lobes at Airy (separated by ~ 9 km) are aligned

with peaks in the surface horizontal magnetic field profile, then the depth of this line source must be ~ 7.8 km. Because we assume an infinitely narrow source, this represents the maximum possible source depth consistent with the hypothesis that the bright lobes align with peaks in the horizontal magnetic field profile. The LP MAG data are too spatially coarse to constrain the distribution of magnetic moments within the source structure so we assign equal strength to each of the 32 dipoles in the array. With the depth fixed and the dipole moment magnitudes set to be equal, the parameter space is reduced to three dimensions (total magnitude, inclination, and declination), allowing for a complete search (varying magnitude in increments of 10^{11} Am 2 and inclination and declination in 1° increments) to find the solution that best fits, in a least squares sense, the LP MAG data. The resulting best fit solution has the dipoles pointed steeply downward (inclination 75° , declination -20°) with total magnetic moment 3.8×10^{12} Am 2 (Table 3). This source model produces a magnetic field pattern at the surface that mimics the morphology of the albedo anomaly, with the field being strongly horizontal in high albedo areas and vertical in the intraswirl dark lane (Figure 11). Remarkably, this same simple source model produces a field pattern at the spacecraft altitude that substantially resembles the LP MAG observations (Figure 12).

4.2.2. Reiner Gamma Model

[25] The Airy model (section 4.2.1) suggests that the dark lane is aligned with a cusp between two peaks in the horizontal magnetic field profile. Based on the Airy example, we may view the two dark lanes at Reiner Gamma as suggestive of cusps in the near-surface horizontal magnetic field profile (see Harnett and Wingfield [2003] for a related discussion). As illustrated in Figure 1d, a horizontally magnetized source will produce strongly horizontal fields directly above the source while producing cusps (where the

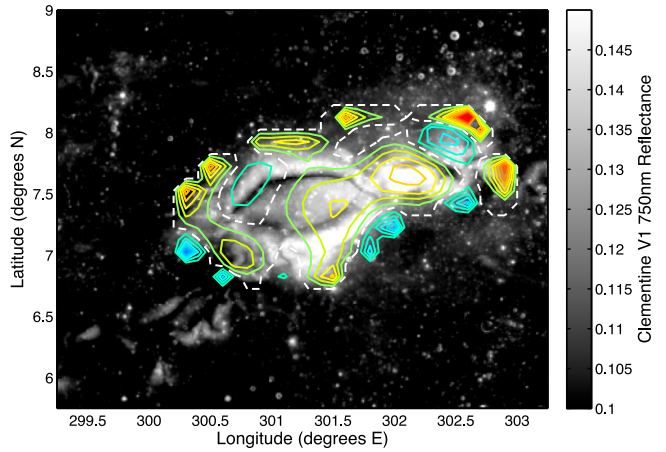


Figure 10. Distribution of source magnetization at Reiner Gamma as estimated by Nicholas et al. [2007] assuming the source layer is 40 km thick. The contour interval is 0.1 A/m with warm colors positive, cool colors negative, and the dashed white contour representing zero magnetization. The contours are superimposed over Clementine V1 750 nm reflectance. Note that our study instead uses Clementine V2 mosaics, which differ in horizontal registration by ~ 7 km in the vicinity of Reiner Gamma.

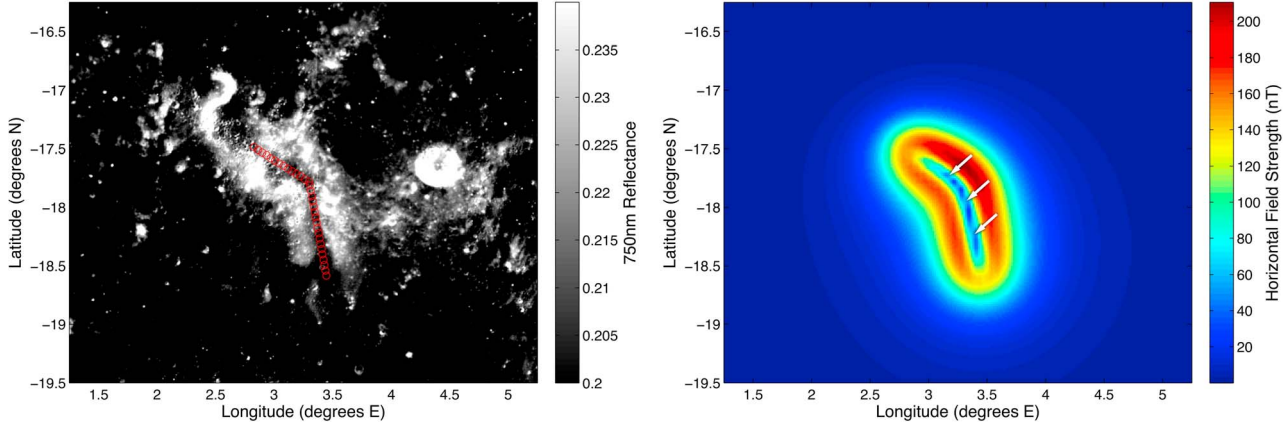


Figure 11. (left) Airy study area showing Clementine albedo map with red circles indicating the locations of the source model's 32 dipoles. (right) Resulting horizontal magnetic field strength predicted at the surface. White arrows indicate where field lines become vertical in the intraswirl dark lane. Figure 12 compares the model field predicted at the spacecraft altitude with the LP MAG observations.

horizontal field strength drops to zero) on either side of the source. This suggests that the horizontally magnetized source material underlies the brightest parts of the Reiner Gamma albedo feature and that the dark lanes may be aligned with the cusps. The appearance of the two dark lanes and the relatively bright material between them may be explained by a superposition of two sources (see Figure 13 and compare with Figure 1).

[26] As with the case illustrated in Figures 1b and 1d, the field illustrated in Figure 13 is strongly horizontal at any altitude over the two horizontally magnetized sources. However, in this case there is an additional region of elevated horizontal field strength where the side lobes interfere constructively between the two sources. Taking this pattern as a cue, we replace the grid of dipoles described in section 4.1.2 with an array of 55 dipoles arranged as curvilinear structures beneath the three brightest parts of the swirl (Figure 14, left). In cross-section, the field pattern from the two approximately linear sources adjacent to the dark lanes resembles the pattern from the two-dipole case illustrated in Figure 13, but the cusps in the horizontal magnetic field profile are shifted outward slightly such that they are displaced laterally (in this case to the north and south) from the center of the sources by a distance equal to the altitude above the source rather than $1/\sqrt{2}$ times the altitude above the source (details are given in Appendix A). If we assume the dark lanes at Reiner Gamma (which are displaced ~ 5 km from the centers of the bright lobes) are aligned with the cusps in the surface horizontal magnetic field profile, then the depth of the source must be ~ 5 km. Because we assume infinitely narrow source structures, this represents the maximum possible source depth consistent with the hypothesis that the dark lanes align with cusps in the horizontal magnetic field profile. The LP MAG data are too spatially coarse to constrain the distribution of magnetic moments within the source structure so we assign equal strength to each of the 55 dipoles in the array. As with the Airy case, we perform a complete search to find the solution that best fits, in a least squares sense, the LP MAG data. The resulting best fit solution has the dipoles pointed with inclination $+2^\circ$ and declination -8° (i.e., pointed nearly horizontally and slightly west of north) and total magnetic moment

$1.0 \times 10^{13} \text{ Am}^2$ (Table 4). This source model produces a magnetic field pattern at the surface that mimics the morphology of the albedo anomaly, with the field being strongly horizontal in high albedo areas and vertical in the intraswirl

Table 3. Final Dipole Array Model for Airy as Described in Section 4.2.1^a

Latitude (°N)	Longitude (°E)	Depth (km)	Magnetic Moment (Am ²)	Inclination (deg)	Declination (deg)
-17.489	2.826	7.8	1.19E+11	75	-20
-17.512	2.862	7.8	1.19E+11	75	-20
-17.534	2.899	7.8	1.19E+11	75	-20
-17.557	2.935	7.8	1.19E+11	75	-20
-17.579	2.972	7.8	1.19E+11	75	-20
-17.602	3.008	7.8	1.19E+11	75	-20
-17.624	3.044	7.8	1.19E+11	75	-20
-17.647	3.081	7.8	1.19E+11	75	-20
-17.669	3.117	7.8	1.19E+11	75	-20
-17.692	3.153	7.8	1.19E+11	75	-20
-17.714	3.190	7.8	1.19E+11	75	-20
-17.737	3.226	7.8	1.19E+11	75	-20
-17.759	3.263	7.8	1.19E+11	75	-20
-17.782	3.299	7.8	1.19E+11	75	-20
-17.815	3.305	7.8	1.19E+11	75	-20
-17.860	3.313	7.8	1.19E+11	75	-20
-17.906	3.322	7.8	1.19E+11	75	-20
-17.951	3.330	7.8	1.19E+11	75	-20
-17.996	3.338	7.8	1.19E+11	75	-20
-18.041	3.347	7.8	1.19E+11	75	-20
-18.087	3.355	7.8	1.19E+11	75	-20
-18.132	3.363	7.8	1.19E+11	75	-20
-18.177	3.372	7.8	1.19E+11	75	-20
-18.223	3.380	7.8	1.19E+11	75	-20
-18.268	3.389	7.8	1.19E+11	75	-20
-18.313	3.397	7.8	1.19E+11	75	-20
-18.359	3.405	7.8	1.19E+11	75	-20
-18.404	3.414	7.8	1.19E+11	75	-20
-18.449	3.422	7.8	1.19E+11	75	-20
-18.494	3.430	7.8	1.19E+11	75	-20
-18.540	3.439	7.8	1.19E+11	75	-20
-18.585	3.447	7.8	1.19E+11	75	-20

^aSee Figure 11. The model consists of 32 dipoles at the indicated latitudes and longitudes, all buried 7.8 km below the surface. The total magnetic moment is $3.8 \times 10^{12} \text{ Am}^2$. Inclination is measured positive downward from the horizontal and declination is measured positive clockwise from north.

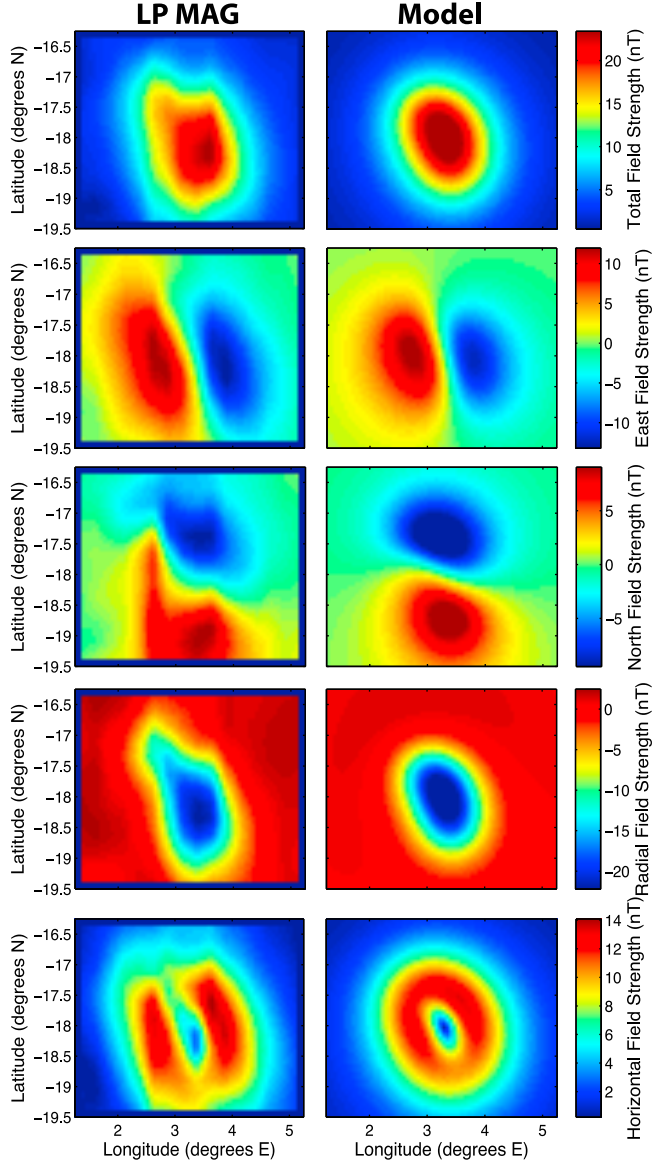


Figure 12. Comparison of (left) the observed field at ~ 18 km over Airy (derived from LP MAG data collected on days 49–50, 77, and 104 of 1999) and (right) the model field (obtained as described in section 4.2.1). Figure 11 shows the horizontal component of the model field predicted at the surface.

dark lanes (Figure 14). Remarkably, this same source model produces a field pattern at the spacecraft altitude that agrees with the Lunar Prospector observations (Figure 15).

5. Discussion

5.1. Magnetization

[27] The models described in section 4.1 suggest that the source material is concentrated under the central parts of the albedo anomalies. Based on the source material distributions illustrated in Figures 6 and 8, we can compute the implied magnetizations at Airy and Reiner Gamma for various assumed layer thicknesses. Figure 16 illustrates that even when the magnetized layer is assumed to be 10 km thick,

typical magnetizations at the Reiner Gamma anomaly are on the order of 1 A/m. If the magnetized layer is only 1 km thick, the implied magnetization approaches 10 A/m at Reiner Gamma. For comparison, *Nicholas et al.* [2007] predict a minimum magnetization of 1 A/m for a layer 1 km thick at Reiner Gamma and *Wieczorek et al.* [2012] calculate ~ 2 A/m for the same layer thickness assuming an anomaly that produces a 10 nT field at 30 km altitude. If we suppose the source structures are further horizontally concentrated, as the albedo-pattern-constrained models of section 4.2 suggest (Figures 11 and 14), the magnetizations would have to be even greater.

5.2. Magnetizing Field

[28] The strong magnetizations at the Airy and Reiner Gamma anomalies could be the result of the source material having cooled in a long lasting global magnetic field, perhaps generated by a core dynamo [*Garrick-Bethell et al.*, 2009;

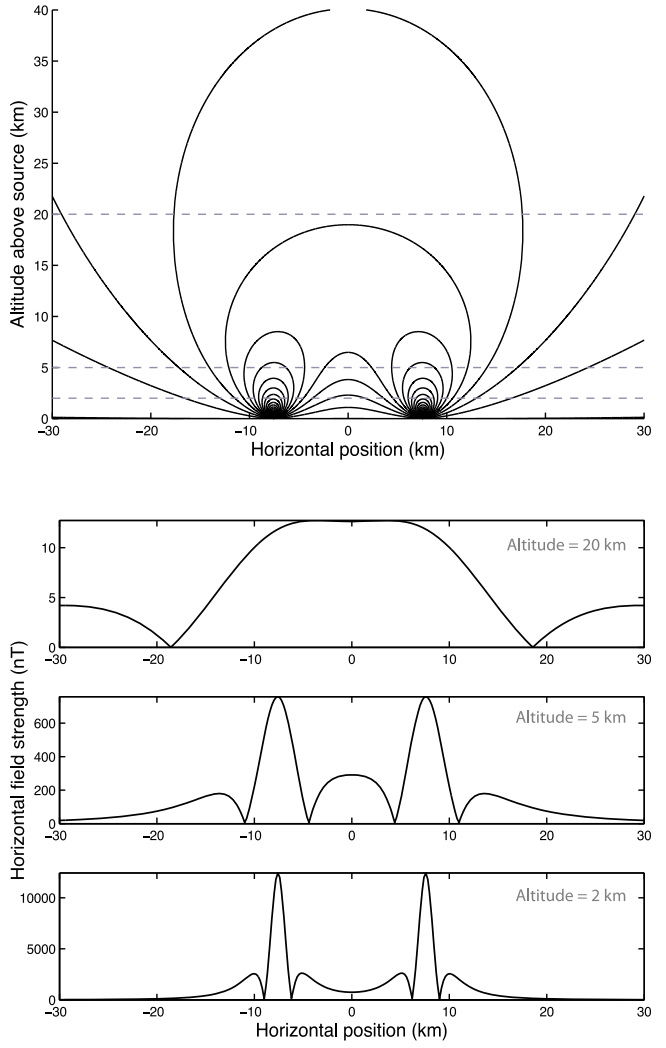


Figure 13. (top) Magnetic field lines due to a pair of dipoles separated by 15 km and oriented horizontally in the plane of the page. (bottom) Profiles of the horizontal component of the magnetic field shown at the various altitudes represented by dashed lines in Figure 13 (top). Each of the dipoles has a magnetic moment of 10^{12} Am 2 .

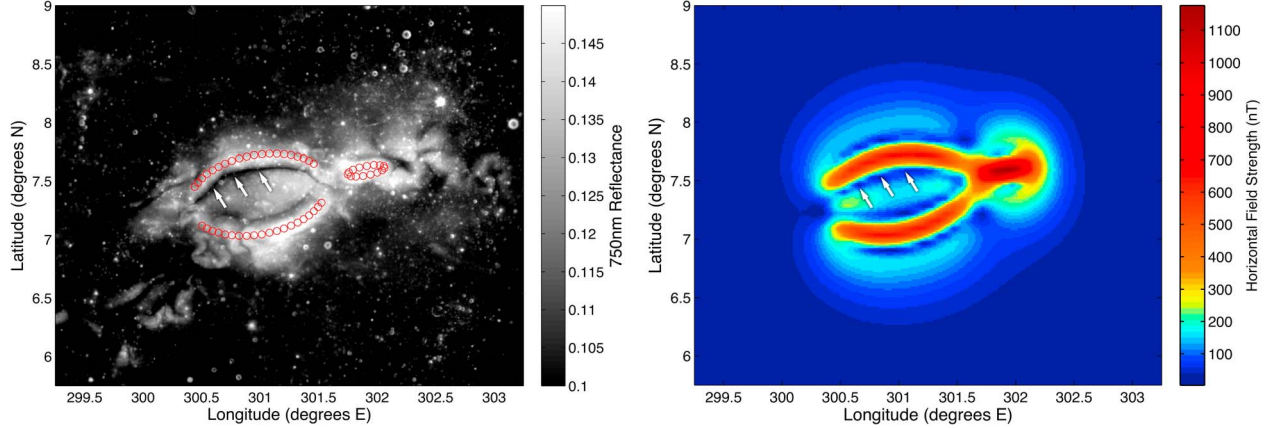


Figure 14. (left) Reiner Gamma study area showing Clementine albedo map with red circles indicating the locations of the source model’s 55 dipoles. (right) Resulting horizontal magnetic field strength predicted at the surface. White arrows indicate where field lines become vertical in one of the intraswirl dark lanes. Figure 15 compares the model field predicted at the spacecraft altitude with the LP MAG observations.

[28] *Dwyer et al., 2011; Le Bars et al., 2011; Shea et al., 2012*. As we have shown here, however, the Airy anomaly (located at approximately 17°S, 3°E) is magnetized with a steep downward inclination while the Reiner Gamma anomaly (located at approximately 7°N, 59°W) is magnetized with almost zero inclination and points approximately toward the north. If these two anomalies acquired their magnetizations by cooling in a dipolar dynamo field, they could not have formed contemporaneously. Instead, the two anomalies may have formed during different global field orientation epochs. Alternatively, the Moon’s dynamo field may have had substantial higher order components (i.e., beyond dipolar).

[29] Another possibility that avoids the difficulties associated with inconsistent magnetization directions is that, rather than being the thermal remanent magnetization signatures of an extinct core dynamo, the Moon’s crustal magnetic anomalies may instead be the result of shock remanent magnetization that occurs following basin-forming impact events when magnetohydrodynamic shock waves converge near the basin antipode producing strong transient fields and potentially magnetizing iron-rich ejecta materials [Hood et al., 2001; Halekas et al., 2001; Richmond et al., 2005; Hood and Artemieva, 2008].

6. Conclusions

[30] Our examination of swirls at Airy and Reiner Gamma, two magnetic anomalies with dissimilar orientation, suggests that magnetic field direction and swirl morphology are related in the way we predict based on the solar wind deflection hypothesis: the Reiner Gamma case delivers evidence that swirls are brightest where magnetic field lines are dominantly horizontal and the Airy case demonstrates a connection between dark lanes and vertically oriented field lines. These findings support the solar wind deflection model for swirl formation, implying that differential solar wind darkening is largely responsible for creating the albedo anomalies. Although our source models do not represent unique solutions, they agree with observational constraints while plausibly accounting for the alternating bright and dark bands at both Airy and Reiner Gamma. Our model results

suggest that swirl morphology could potentially be used to infer small-scale structure in the near-surface magnetic field as well as the layout and burial depth of the magnetic source material. For Airy and Reiner Gamma, we infer maximum source burial depths of ~8 km and ~5 km, respectively, and horizontally concentrated sources with strong magnetizations (~10 A/m or greater for a layer 1 km thick). Examination of additional swirls may help to further our understanding of how magnetic field direction relates to swirl morphology, but ultimately, very near-surface magnetic field and solar wind flux measurements (i.e., from altitudes of hundreds of meters or less) will be required to confirm our predictions.

Appendix A: Magnetic Field Profile Calculations

[31] Here, we calculate the locations of the maxima and minima in the horizontal magnetic field profiles due to both vertically and horizontally magnetized sources. We first consider the single dipole sources illustrated in Figure 1 and then repeat the calculations for the line sources discussed in section 4.

A1. Single Dipole Source

[32] If we take the horizontal and vertical positions in Figures 1a and 1b to be the x and z coordinates, respectively, and if the magnetic dipoles are each located at the origin with magnitude and orientation represented by a vector, \mathbf{m} , then the resulting magnetic field, \mathbf{B} , at a position, $\mathbf{r} = (x\hat{\mathbf{x}} + y\hat{\mathbf{y}} + z\hat{\mathbf{z}})$, is given by:

$$\mathbf{B} = \frac{\mu_0}{4\pi} \nabla \cdot (\mathbf{m} \cdot \mathbf{r}) \mathbf{r} - \mathbf{m} r^2 \frac{\nabla}{r^5} \frac{1}{r^5} \quad (\text{A1})$$

Equation (A1) is adapted from Blakely [1995, p. 75]. Here, we employ SI units with μ_0 being the magnetic permeability of free space. For points in the x-z plane, the horizontal component of the magnetic field (B_h) is identical to the magnitude of the x-component (B_x) since, by symmetry, magnetic field lines cannot cross the x-z plane (i.e., cannot have a y-component). Considering the case of the vertically

Table 4. Final Dipole Array Model for Reiner Gamma as Described in Section 4.2.2^a

Latitude (°N)	Longitude (°E)	Depth (km)	Magnetic Moment (Am ²)	Inclination (deg)	Declination (deg)
7.649	301.460	5	1.82E+11	2	-8
7.673	301.418	5	1.82E+11	2	-8
7.693	301.371	5	1.82E+11	2	-8
7.710	301.320	5	1.82E+11	2	-8
7.723	301.264	5	1.82E+11	2	-8
7.731	301.205	5	1.82E+11	2	-8
7.735	301.144	5	1.82E+11	2	-8
7.735	301.080	5	1.82E+11	2	-8
7.731	301.015	5	1.82E+11	2	-8
7.723	300.950	5	1.82E+11	2	-8
7.710	300.885	5	1.82E+11	2	-8
7.693	300.821	5	1.82E+11	2	-8
7.673	300.759	5	1.82E+11	2	-8
7.649	300.700	5	1.82E+11	2	-8
7.622	300.645	5	1.82E+11	2	-8
7.592	300.593	5	1.82E+11	2	-8
7.559	300.546	5	1.82E+11	2	-8
7.525	300.505	5	1.82E+11	2	-8
7.488	300.469	5	1.82E+11	2	-8
7.451	300.439	5	1.82E+11	2	-8
7.315	301.525	5	1.82E+11	2	-8
7.278	301.495	5	1.82E+11	2	-8
7.241	301.459	5	1.82E+11	2	-8
7.207	301.418	5	1.82E+11	2	-8
7.174	301.371	5	1.82E+11	2	-8
7.144	301.319	5	1.82E+11	2	-8
7.117	301.264	5	1.82E+11	2	-8
7.093	301.205	5	1.82E+11	2	-8
7.073	301.144	5	1.82E+11	2	-8
7.056	301.080	5	1.82E+11	2	-8
7.043	301.015	5	1.82E+11	2	-8
7.035	300.949	5	1.82E+11	2	-8
7.031	300.884	5	1.82E+11	2	-8
7.031	300.820	5	1.82E+11	2	-8
7.035	300.759	5	1.82E+11	2	-8
7.043	300.700	5	1.82E+11	2	-8
7.056	300.644	5	1.82E+11	2	-8
7.073	300.593	5	1.82E+11	2	-8
7.093	300.546	5	1.82E+11	2	-8
7.117	300.504	5	1.82E+11	2	-8
7.542	301.774	5	1.82E+11	2	-8
7.538	301.819	5	1.82E+11	2	-8
7.543	301.878	5	1.82E+11	2	-8
7.555	301.943	5	1.82E+11	2	-8
7.573	302.001	5	1.82E+11	2	-8
7.593	302.043	5	1.82E+11	2	-8
7.612	302.062	5	1.82E+11	2	-8
7.628	302.056	5	1.82E+11	2	-8
7.636	302.024	5	1.82E+11	2	-8
7.637	301.973	5	1.82E+11	2	-8
7.629	301.910	5	1.82E+11	2	-8
7.615	301.847	5	1.82E+11	2	-8
7.596	301.794	5	1.82E+11	2	-8
7.576	301.759	5	1.82E+11	2	-8
7.557	301.749	5	1.82E+11	2	-8

^aSee Figure 14. The model consists of 55 dipoles at the indicated latitudes and longitudes, all buried 5 km below the surface. The total magnetic moment is 1.0×10^{13} Am². Inclination is measured positive downward from the horizontal and declination is measured positive clockwise from north.

oriented dipole ($\mathbf{m} = [0 \ 0 \ m]^T$), the horizontal component of the magnetic field becomes:

$$\mathbf{B}_h = |\mathbf{B}_x| = \frac{\mathbf{m}_\theta}{4\mu_0} \cdot \frac{(3mzx)}{(x^2 + z^2)^{5/2}} \quad (\text{A2})$$

Equation (A2) demonstrates that field lines directly over a vertically oriented dipole are vertical at any altitude because $B_h = 0$ when $x = 0$ (this is also evident in Figure 1a). Differentiating equation (A2) with respect to x and setting the result to zero yields the positions of the peaks in the horizontal field strength profile:

$$x_{B_{h\max}} = \pm \frac{1}{2}z \quad (\text{A3})$$

This means that the separation between peaks ($2x$) is equal to the altitude above the source (z), which is evident in Figure 1c.

[33] Considering the case of the horizontally oriented dipole ($\mathbf{m} = [m \ 0 \ 0]^T$), and still being restricted to points in

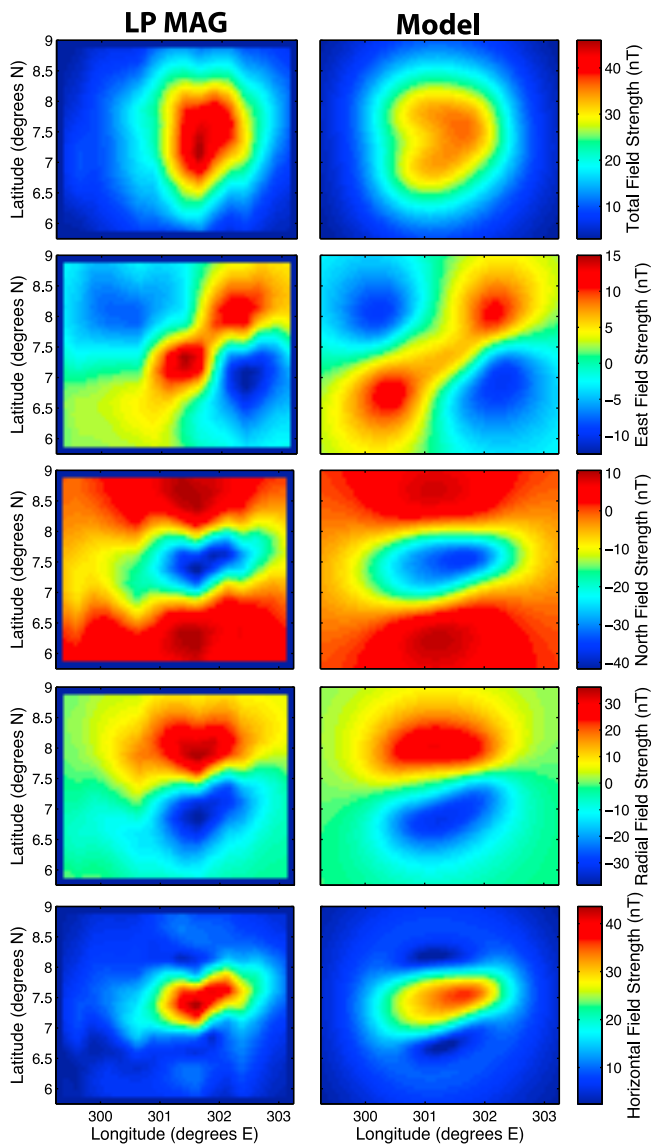


Figure 15. Comparison of (left) the observed field at ~18 km over Reiner Gamma (derived from LP MAG data collected on days 54, 81–82, and 109 of 1999) and (right) the model field (obtained as described in section 4.2.2). Figure 14 shows the horizontal component of the model field predicted at the surface.

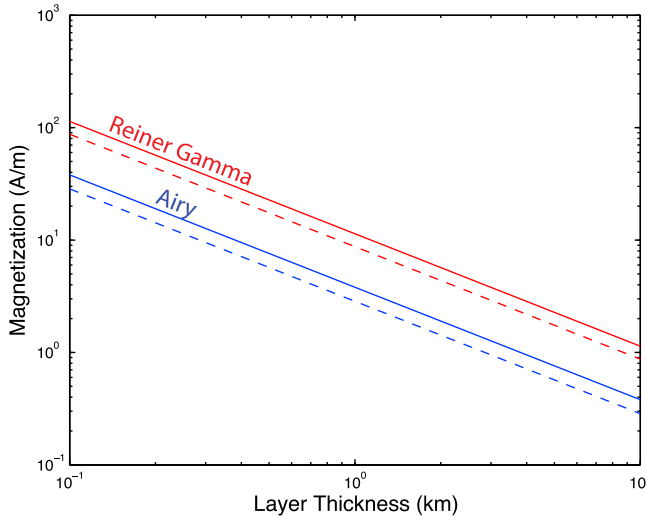


Figure 16. Rock magnetization implied by source models illustrated in Figures 6 and 8 versus assumed layer thickness. Solid lines are based on the maximum individual dipole moments found in those models ($\sim 2.1 \times 10^{11} \text{ Am}^2$ for Airy, $\sim 6.5 \times 10^{11} \text{ Am}^2$ for Reiner Gamma), and the dashed lines are based on characteristic values of $1.25 \times 10^{11} \text{ Am}^2$ for Airy and $3.4 \times 10^{11} \text{ Am}^2$ for Reiner Gamma.

the x-z plane, the vertical (z) component of the magnetic field becomes:

$$B_v = |B_z| = \frac{m_0}{4\pi} \frac{(3mxz)}{(x^2 + z^2)^{\frac{5}{2}}} \quad (\text{A4})$$

Equation (A4) demonstrates that field lines directly over a horizontally oriented dipole are horizontal at any altitude because $B_z = 0$ when $x = 0$ (Figure 1b). Again, starting from equation (A1), and considering only points in the x-z plane, the horizontal component of the magnetic field due to a horizontally oriented dipole that is aligned with the x axis becomes:

$$B_h = |B_x| = \frac{m_0}{4\pi} \frac{(m(2x^2 - z^2))}{(x^2 + z^2)^{\frac{5}{2}}} \quad (\text{A5})$$

Setting equation (A5) to zero shows that the horizontal field strength drops to zero when:

$$x_{B_h=0} = \pm \frac{1}{\sqrt{2}} \quad (\text{A6})$$

Hence, the cusps in the horizontal magnetic field profile are laterally displaced from the source by a distance of $1/\sqrt{2}$ times the altitude above the source (this is evident in Figure 1d).

A2. Linear Source

[34] Imagine that instead of a single dipole, the source is a linear structure such as a long, uniformly magnetized cylinder. If this linear source is infinitely long and coincident with

the y axis, and the magnetization per unit length is m' , then the magnetic field is given by:

$$B = \frac{m_0}{4\pi} \frac{(\square)}{4(m' \cdot r)r - 2m'r^2} \frac{1}{r^4} \quad (\text{A7})$$

Equation (A7) is adapted from Blakely [1995, p. 96]. Again, considering only points in the x-z plane, the horizontal component of the magnetic field due to the vertically magnetized line source becomes:

$$B_h = |B_x| = \frac{m_0}{4\pi} \frac{(\frac{4m'zx}{(x^2 + z^2)^2})}{(\text{A8})}$$

As with the dipole case, field lines directly over a vertically magnetized line source are vertical at any altitude. Differentiating equation (A8) with respect to x and setting the result to zero yields the positions of the peaks in the horizontal field profile:

$$x_{B_{h\max}} = \pm \frac{1}{\sqrt{3}} \quad (\text{A9})$$

Considering the case of a horizontally magnetized line source, the vertical (z) component of the magnetic field becomes:

$$B_v = |B_z| = \frac{m_0}{4\pi} \frac{(\frac{4m'xz}{(x^2 + z^2)^2})}{(\text{A10})}$$

Hence, field lines directly over a horizontally magnetized linear source are horizontal at any altitude. Again, starting from equation (A7), and considering only points in the x-z plane, the horizontal component of the magnetic field due to a linear source coincident with the y axis and magnetization parallel to the x axis becomes:

$$B_h = |B_x| = \frac{m_0}{4\pi} \frac{(\frac{2m'(x^2 - z^2)}{(x^2 + z^2)^2})}{(\text{A11})}$$

Setting equation (A11) to zero shows that the horizontal field strength drops to zero when:

$$x_{B_h=0} = \pm z \quad (\text{A12})$$

Hence, the cusps in the horizontal magnetic field profile are laterally displaced from the line source by a distance equal to the altitude above the source.

Appendix B: Genetic Search Algorithm

[35] The magnetic source models discussed in section 4.1 were obtained using a heuristic search technique known as

Table B1. The 211 ‘Genes’ That Define an Individual Source Model

Gene Number	Controls
1	Dipole grid burial depth (km)
2	Magnetic moment inclination (deg)
3	Magnetic moment declination (deg)
4	Magnitude of dipole #1 (Am^2)
...	...
211	Magnitude of dipole #208 (Am^2)

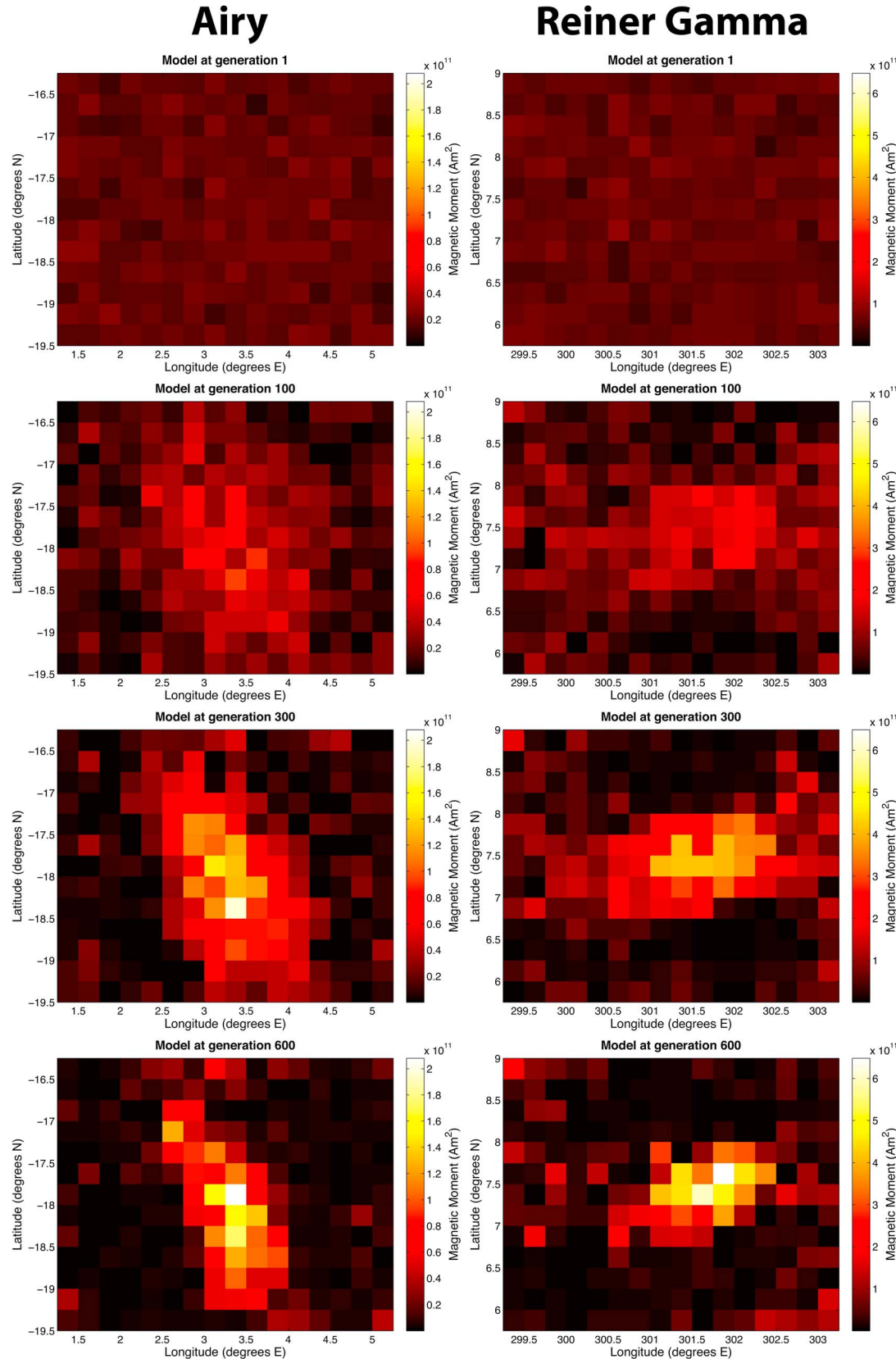


Figure B1. Snapshots at generations 1, 100, 300, and 600 during the evolution of the dipole grid source models for (left) Airy and (right) Reiner Gamma. Each panel shows the distribution of magnetic moments from the best-performing model of the specified generation.

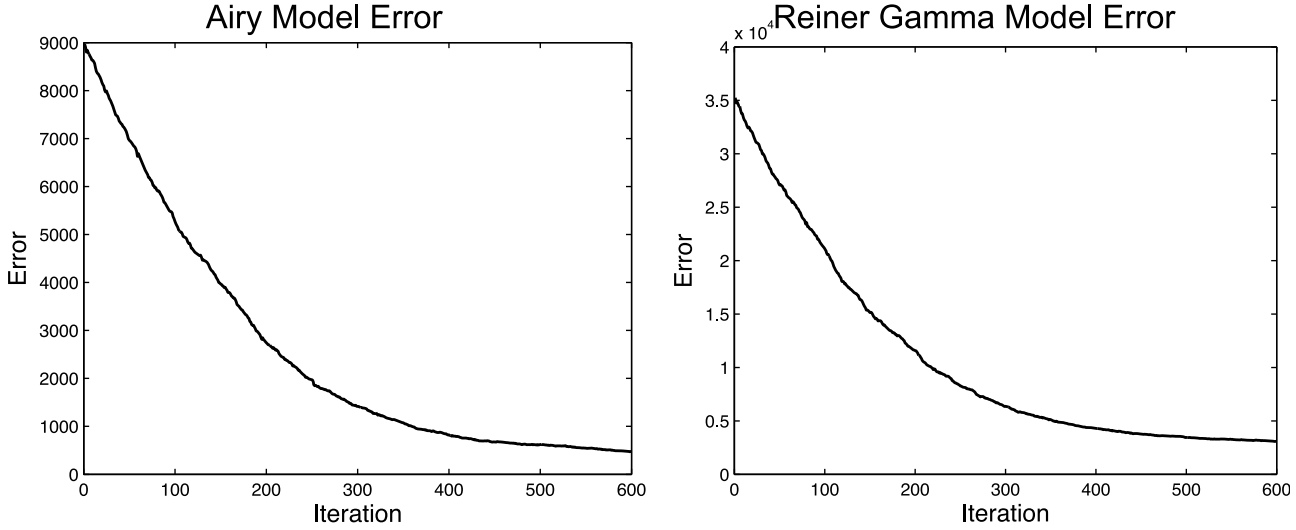


Figure B2. Evolution of dipole grid source model error over 600 generations for (left) Airy and (right) Reiner Gamma. The error shown is the sum of squared ‘effective’ errors (as described in section 4.1.1) over all LP MAG data points for the best-performing model in each generation.

a genetic algorithm. Genetic algorithms have a diverse range of applications [Holland, 1992; Goldberg, 1989] including large-scale optimization problems such as ours: to find a source model (defined by 211 parameters) that produces minimal error between predicted and observed magnetic fields. Genetic algorithms employ concepts borrowed from gene-centered biological evolution [Dawkins, 1976] in order to iteratively (i.e., over many generations) progress toward solutions with increasing degrees of ‘fitness’. In our case, this ‘fitness’ is a measure of how well the magnetic field produced by the source model matches the Lunar Prospector magnetometer (LP MAG) observations.

[36] Our algorithm begins by generating a population of individual source models with randomly distributed characteristics. The characteristics of each individual source model are defined by its ‘genes’, with each individual having the 211 distinct genes listed in Table B1. At each iteration, or generation, the individual members of the population are evaluated according to how well they predict the magnetic field at each of the LP MAG observation points. We compute the error between the prediction and the observation using the ‘effective error’ metric described in section 4.1.1. We then rank the individuals from lowest to highest sum of squared effective errors. The individuals with the lowest errors are then selected as the ‘parents’ of the next generation. The next iteration begins by generating a new population to replace the previous generation. Each individual in the new generation is formed by setting each of its 211 genes equal to the corresponding gene from one of its parents in a process known as crossover (analogous to chromosomal crossover). For example, an individual’s gene for inclination will match the inclination gene of one of its parents (chosen at random from among the parents). Because only the best-performing individuals contribute their genes to the next generation, individuals of each new generation tend to inherit the best characteristics of the previous generation. We then apply random mutations (i.e., randomly adjust several isolated

genes). This step ensures variation in the population and allows for the possibility of introducing advantageous genes not possessed by the parents. Finally, members of the new generation are evaluated and their best performers are selected as the parents of the next generation. With each generation, genes that result in large model errors tend to be discarded while genes that result in smaller model errors tend to be retained. Inheritance and selection lead the gene pool to be increasingly rich in genes that form good source models while crossover and mutations ensure variation, allowing for innovations that can lead offspring to outperform their parents. The result is that the population progresses gradually toward optimality in terms of minimum model error.

[37] While this explanation captures the essence of the algorithm, our implementation includes additional details such as gene mutation rate (the probability that any given gene will mutate) and how “random” mutations are distributed (i.e., it is not useful to have sudden changes in burial depth on the order of 1000 km, for example, so mutations must be limited to reasonable adjustments according to some distribution). We experimented with various population sizes and numbers of parents selected at each generation (there must be at least two parents but more than two is also allowed). For computational efficiency, a small population size is preferred. The algorithm was found to operate effectively with a population of just 10 individuals in which the top-performing 3 contribute their genes to the next generation. We allow mutations to occur with a probability of 0.1 and when they do occur, the gene is adjusted from its current value according to a normal distribution with some pre-defined standard deviation (which depends on whether the gene has units of kilometers, degrees or Am^2). We also apply smaller mutations with a higher probability in order to ensure a measurable degree of variation in the population. The initial population is generated based on a seed model; each individual in the initial population is formed by applying normally distributed adjustments to each of the genes in

the seed model. While the choice of seed model and parameter settings influences the efficiency of the algorithm (i.e., how quickly it reaches a good solution), the end results tend to be very similar across a wide range of parameters and initial conditions. For the dipole grid source models presented in section 4.1, the algorithm was allowed to iterate through 600 generations (Figure B1). Based on the trends in error evolution (Figure B2), we would not expect additional iterations to yield substantial improvements.

[38] **Acknowledgments.** This research was performed as part of the World Class University Project at Kyung Hee University and sponsored by the Korean Ministry of Education, Science and Technology. Additional support was provided by the NASA Ames Research Center/University of California Santa Cruz University Affiliated Research Center. We would like to thank Lon Hood, Robert Lin, Jasper Halekas, Greg Delory, Robert Lillis, and Michael Purucker for their comments and suggestions and Joseph Nicholas for the data used to generate Figure 10.

References

- Archinal, B. B. A., M. R. Rosiek, R. L. Kirk, and B. L. Redding (2006), The Unified Lunar Control Network 2005, *U.S. Geol. Surv. Open File Rep., 2006-1367*.
- Blakely, R. J. (1995), *Potential Theory in Gravity and Magnetic Applications*, Cambridge Univ. Press, Cambridge, U. K., doi:10.1017/CBO9780511549816.
- Blewett, D. T., B. R. Hawke, N. C. Richmond, and C. G. Hughes (2007), A magnetic anomaly associated with an albedo feature near Airy crater in the lunar nearside highlands, *Geophys. Res. Lett.*, **34**, L24206, doi:10.1029/2007GL031670.
- Blewett, D. T., E. I. Coman, B. R. Hawke, J. J. Gillis-Davis, M. E. Purucker, and C. G. Hughes (2011), Lunar swirls: Examining crustal magnetic anomalies and space weathering trends, *J. Geophys. Res.*, **116**, E02002, doi:10.1029/2010JE003656.
- Coleman, P. J., B. R. Lichtenstein, C. T. Russell, L. R. Sharp, and G. Schubert (1972), Magnetic fields near the moon, *Proc. Lunar Sci. Conf., 3rd*, 2271–2286.
- Dawkins, R. (1976), *The Selfish Gene*, Oxford Univ. Press, Oxford, U. K.
- Dwyer, C. A., D. J. Stevenson, and F. Nimmo (2011), A long-lived lunar dynamo driven by continuous mechanical stirring, *Nature*, **479**(7372), 212–214, doi:10.1038/nature10564.
- Dyal, P., C. W. Parkin, and C. P. Sonett (1970), Apollo 12 Magnetometer: Measurement of a steady magnetic field on the surface of the Moon, *Science*, **169**(3947), 762–764, doi:10.1126/science.169.3947.762.
- Dymond, J., and J. Arkani-Hamed (1998), Equivalent source magnetic dipoles revisited, *Geophys. Res. Lett.*, **25**(11), 2003–2006, doi:10.1029/98GL51331.
- Garrick-Bethell, I., B. P. Weiss, D. L. Shuster, and J. Buz (2009), Early lunar magnetism, *Science*, **323**(5912), 356–359, doi:10.1126/science.1166804.
- Garrick-Bethell, I., J. W. Head, and C. M. Pieters (2011), Spectral properties, magnetic fields, and dust transport at lunar swirls, *Icarus*, **212**(2), 480–492, doi:10.1016/j.icarus.2010.11.036.
- Goldberg, D. (1989), *Genetic Algorithms in Search, Optimization and Machine Learning*, Addison-Wesley, Reading, Mass.
- Halekas, J. S., D. L. Mitchell, R. P. Lin, S. Frey, L. L. Hood, M. H. Acuña, and A. B. Binder (2001), Mapping of crustal magnetic anomalies on the lunar near side by the Lunar Prospector electron reflectometer, *J. Geophys. Res.*, **106**(E11), 27,841–27,852, doi:10.1029/2000JE001380.
- Hapke, B. (2001), Space weathering from Mercury to the asteroid belt, *J. Geophys. Res.*, **106**(E5), 10,039–10,073, doi:10.1029/2000JE001338.
- Harnett, E. M., and R. M. Winglee (2003), 2.5-D fluid simulations of the solar wind interacting with multiple dipoles on the surface of the Moon, *J. Geophys. Res.*, **108**(A2), 1088, doi:10.1029/2002JA009617.
- Holland, J. (1992), *Adaptation in Natural and Artificial Systems: An Introductory Analysis with Applications to Biology, Control, and Artificial Intelligence*, MIT Press, Cambridge, Mass.
- Hood, L. L. (2011), Central magnetic anomalies of Nectarian-aged lunar impact basins: Probable evidence for an early core dynamo, *Icarus*, **211**(2), 1109–1128, doi:10.1016/j.icarus.2010.08.012.
- Hood, L. L., and N. A. Artemieva (2008), Antipodal effects of lunar basin-forming impacts: Initial 3D simulations and comparisons with observations, *Icarus*, **193**(2), 485–502, doi:10.1016/j.icarus.2007.08.023.
- Hood, L. L., and G. Schubert (1980), lunar magnetic anomalies and surface optical properties, *Science*, **208**, 49–51, doi:10.1126/science.208.4439.49.
- Hood, L. L., and C. R. Williams (1989), The lunar swirls: Distribution and possible origins, *Proc. Lunar Planet. Sci. Conf., 19th*, 99–113.
- Hood, L. L., P. J. Coleman, and D. E. Wilhelms (1979), Lunar nearside magnetic anomalies, in *Proc. Lunar Planet. Sci. Conf., 10th*, 2235–2257.
- Hood, L. L., C. T. Russell, and P. Coleman (1981), Contour maps of lunar remanent magnetic fields, *J. Geophys. Res.*, **86**, 1055–1069, doi:10.1029/JB086iB02p01055.
- Hood, L. L., A. Zakharian, J. Halekas, D. L. Mitchell, R. P. Lin, M. H. Acuña, and A. B. Binder (2001), Initial mapping and interpretation of lunar crustal magnetic anomalies using Lunar Prospector magnetometer data, *J. Geophys. Res.*, **106**(E11), 27,825–27,839, doi:10.1029/2000JE001366.
- Kramer, G. Y., et al. (2011), M^3 spectral analysis of lunar swirls and the link between optical maturation and surface hydroxyl formation at magnetic anomalies, *J. Geophys. Res.*, **116**, E00G18, doi:10.1029/2010JE003729.
- Kurata, M., H. Tsunakawa, Y. Saito, H. Shibuya, M. Matsushima, and H. Shimizu (2005), Mini-magnetosphere over the Reiner Gamma magnetic anomaly region on the Moon, *Geophys. Res. Lett.*, **32**, L24205, doi:10.1029/2005GL024097.
- Le Bars, M., M. A. Wieczorek, Ö. Karatekin, D. Cébron, and M. Laneuville (2011), An impact-driven dynamo for the early Moon, *Nature*, **479**(7372), 215–218, doi:10.1038/nature10565.
- Lin, R. P. (1979), Constraints on the origins of lunar magnetism from electron reflection measurements of surface magnetic fields, *Phys. Earth Planet. Inter.*, **20**, 271–280, doi:10.1016/0031-9201(79)90050-5.
- Lin, R. P., D. L. Mitchell, D. W. Curtis, K. A. Anderson, C. W. Carlson, J. McFadden, M. H. Acuña, L. L. Hood, and A. Binder (1998), Lunar surface magnetic fields and their interaction with the solar wind: Results from lunar prospector, *Science*, **281**(5382), 1480–1484, doi:10.1126/science.281.5382.1480.
- Neish, C. D., D. T. Blewett, D. B. J. Bussey, S. J. Lawrence, M. Mechtley, and B. J. Thomson (2011), The surficial nature of lunar swirls as revealed by the Mini-RF instrument, *Icarus*, **215**(1), 186–196, doi:10.1016/j.icarus.2011.06.037.
- Ness, N. F., K. W. Behannon, C. S. Scearce, and S. C. Cantarano (1967), Early results from the magnetic field experiment on Lunar Explorer 35, *J. Geophys. Res.*, **72**(23), 5769–5778, doi:10.1029/JZ072i023p05769.
- Nicholas, J. B., M. E. Purucker, and T. J. Sabaka (2007), Age spot or youthful marking: Origin of Reiner Gamma, *Geophys. Res. Lett.*, **34**, L02205, doi:10.1029/2006GL027794.
- Parker, R. L. (2003), Ideal bodies for Mars magnetics, *J. Geophys. Res.*, **108**(E1), 5006, doi:10.1029/2001JE001760.
- Pieters, C. M., et al. (2009), Character and spatial distribution of OH/H₂O on the surface of the Moon seen by M^3 on Chandrayaan-1, *Science*, **326**(5952), 568–572, doi:10.1126/science.1178658.
- Pinet, P. C., V. V. Shevchenko, S. D. Chevrel, Y. Dayou, and C. Rosenberg (2000), Local and regional lunar regolith characteristics at Reiner Gamma Formation: Optical and spectroscopic properties from Clementine and Earth-based data, *J. Geophys. Res.*, **105**(E4), 9457–9475, doi:10.1029/1999JE001086.
- Purucker, M. (2008), A global model of the internal magnetic field of the Moon based on Lunar Prospector magnetometer observations, *Icarus*, **197**(1), 19–23, doi:10.1016/j.icarus.2008.03.016.
- Purucker, M. E., and J. B. Nicholas (2010), Global spherical harmonic models of the internal magnetic field of the Moon based on sequential and coestimation approaches, *J. Geophys. Res.*, **115**, E12007, doi:10.1029/2010JE003650.
- Purucker, M. E., T. J. Sabaka, and R. A. Langel (1996), Conjugate gradient analysis: A new tool for studying satellite magnetic data sets, *Geophys. Res. Lett.*, **23**(5), 507–510, doi:10.1029/96GL00388.
- Richmond, N. C., L. L. Hood, D. L. Mitchell, R. P. Lin, M. H. Acuña, and A. B. Binder (2005), Correlations between magnetic anomalies and surface geology antipodal to lunar impact basins, *J. Geophys. Res.*, **110**, E05011, doi:10.1029/2005JE002405.
- Schultz, P. H., and L. J. Smrk (1980), Cometary collisions on the Moon and Mercury, *Nature*, **284**, 22–26, doi:10.1038/284022a0.
- Shea, E. K., B. P. Weiss, W. S. Cassata, D. L. Shuster, S. M. Tikoo, J. Gattaccea, T. L. Grove, and M. D. Fuller (2012), A long-lived lunar core dynamo, *Science*, **335**(6067), 453–456, doi:10.1126/science.1215359.
- Shibuya, H., H. Tsunakawa, F. Takahashi, H. Shimizu, and M. Matsushima (2010), Near surface magnetic field mapping over the swirls in the SPA region using Kaguya LMG data, *EPSC Abstr.*, **5**, Abstract EPSC2010-166.
- Smith, D. E., et al. (2010), Initial observations from the Lunar Orbiter Laser Altimeter (LOLA), *Geophys. Res. Lett.*, **37**, L18204, doi:10.1029/2010GL043751.
- Starukhina, L. V., and Y. G. Shkuratov (2004), Swirls on the Moon and Mercury: Meteoroid swarm encounters as a formation mechanism, *Icarus*, **167**(1), 136–147, doi:10.1016/j.icarus.2003.08.022.

- Vernazza, P., R. P. Binzel, A. Rossi, M. Fulchignoni, and M. Birlan (2009), Solar wind as the origin of rapid reddening of asteroid surfaces, *Nature*, 458(7241), 993–995, doi:10.1038/nature07956.
- Von Frese, R. R. B., W. J. Hinze, and L. W. Braile (1981), Spherical Earth gravity and magnetic anomaly analysis by equivalent point source inversion, *Earth Planet. Sci. Lett.*, 53, 69–83, doi:10.1016/0012-821X(81)90027-3.
- Wieczorek, M. A., B. P. Weiss, and S. T. Stewart (2012), An impactor origin for lunar magnetic anomalies, *Science*, 335(6073), 1212–1215, doi:10.1126/science.1214773.

